Bimetallic RuNi nanoparticles as catalysts for upgrading biomass: metal dilution and solvent effects on selectivity shifts

Miquel Cardona-Farreny,[a] Pierre Lecante,[b] Jerome Esvan,[c] Chiara Dinoi,[d] Iker del Rosal,[d] Romuald Poteau,[d] Karine Philippot,[a] M. Rosa Axet[a*]

[a] *CNRS, LCC (Laboratoire de Chimie de Coordination), Université de Toulouse, UPS, INPT, 205 route de Narbonne, BP 44099, F-31077 Toulouse Cedex 4, France*

[b] *Centre d'élaboration des matériaux et d'études structurales UPR CNRS 8011, 29 Rue Jeanne-Marvig, BP 4347, 31055 Toulouse, France*

[c] *CIRIMAT, Université de Toulouse, CNRS-INPT-UPS, 4 Allée Emile Monso, BP 44362, 31030 Toulouse, France*

[d] *INSA–CNRS–UPS, LPCNO, Université Fédérale de Toulouse Midi-Pyrénées, 135 Avenue de Rangueil, F-31077 Toulouse, France*

Abstract

RuNi nanoparticles (NP) were prepared by decomposition of [Ru(η^4-C_8H_{12})(η^6-C_8H_{10})] and [Ni(η^4-C_8H_{12})$_2$] by H_2 in the presence of polyvinylpyrrolidone (PVP) at 85°C using several Ru/Ni ratios. The nanoparticles display a segregated structure in which Ni is on the surface, as ascertained by wide angle X-ray scattering (WAXS). The catalytic activity in the selective hydrogenation of furfural of these RuNi NP was correlated to the Ru content. High selectivity towards the partially hydrogenated product 2-(hydroxymethyl)furan (HF), was found when carrying out the reaction in tetrahydrofuran (THF). A different scenario was found when using a protic polar solvent, 1-propanol. Catalyst displaying Ru on the surface, were able to hydrogenate the heteroaromatic ring, while those with Ni on the surface were highly selective towards the partially hydrogenated product. In addition, Ru surfaces were prone to catalyse the acetalization reaction in the presence of the alcoholic solvent, while the addition of Ni supressed this reactivity. Density functional theory (DFT) calculations performed on hydrogenated Ru nanoparticles ($Ru_{55}H_{70}$) show differences on the adsorption energies of several reagents, products, reaction intermediates, and solvents onto the Ru NP surface, which are in line with the experimental catalytic results.

Introduction

Nanoalloys constituted by several metals, often bimetallic, but also trimetallic and more, represent a promising set of materials for several applications, and in particular, for catalysis they can provide an improved reactivity when compared to the analogous single metal counterparts.[1-3] Nanoalloys have been extensively studied in catalysis, in areas such as oil refineries, automobile exhaust gas cleaning, petrochemical manufacturing, fine chemical synthesis, and electrocatalytic and photocatalytic, hydrogen evolution reactions.[4-6] The characteristics of the bimetallic nanoparticles (NP) are

determined by the differences of properties between metals composing the bimetallic NP, such as electron negativity or ionization potentials, but also by the chemical order (alloy, core-shell, among others) of metals, together with size and shape, of the final NP.[1-3] Ruthenium based heterogeneous catalysts,[7-9] and in particular Ru based colloidal NP[10] have interesting catalytic properties exploited in a variety of reactions, such as reductions, oxidations, Fisher-Tropsch, among others. Even if Ru is not among the most expensive rare metals, its combination with an economical and more abundant metal, together with the possibility to produce synergistic effects with it, is an interesting viewpoint in terms of economics and performance perspectives. The combination of Ni with Ru provides to the rare metal different electronic properties as it has been shown by X-ray photoelectron spectroscopy (XPS).[11-13] even if the material is composed of independent monometallic NP of Ru and Ni in close vicinity.[14,15] In this latter case, resulting synergetic effects between both metals have been observed. It has been also proposed that Ru is able to reduce Ni^{2+} through hydrogen spillover.[16,17] Thus, aside of the electronic effects, the hydride mobility could imply enhanced catalytic reactivity for RuNi NP. Several structures have been described for RuNi based catalysts, homogenous alloyed structure,[18,19] core-shell, with both Ru[20] or Ni[21] on the core, and others.[20] RuNi based catalysts have been successfully used in methanation of CO and CO_2,[22-35] steam and dry reforming of methane,[36-42] conversion of biomass into valuable chemicals,[14-16,20,43,44] dehydrogenation of ammonia borane,[18,45-50] hydrogenation,[19,51-58] and others.[11,13,59-61] Synergetic effects between Ru and Ni have been found in RuNi based catalysts when applied to hydrodeoxygenation or hydrogenation reactions.[14-16,19,20,44,54] This synergy may be tuned thought the nanostructure of the bimetallic catalysts,[57] or the metal-metal ratio.[19,20,44,52] The control over the proportion of both metals in the bimetallic NP is an interesting approach to control the catalytic properties. For instance, a volcano-type relation between Ru/Ni ratio and selectivity in the hydrogenolysis of 2-phenoxy-1-phenethanol was found, in which $Ni_{85}Ru_{15}$ displayed the best selectivity towards the production of monomeric products.[20] The decomposition of organometallic complexes under H_2 pressure is a versatile tool to obtain NP of specific characteristics.[62] Size, shape, composition, chemical order and surface compounds may be modulated straightforward. Bimetallic NP with interesting catalytic properties are obtained as well using this methodology.[63,64] Herein, we report the synthesis of RuNi NP, their characterization, and their use as catalysts in the selective hydrogenation of furfural. Some of the catalytic experimental results are supported by DFT calculations. The $Ru_{55}H_{70}$ model has been chosen to evaluate the adsorption energies of the solvents, reagents, products, and reaction intermediates, present in the furfural hydrogenation reaction. The results allow us to propose plausible reaction pathways for both the hydrogenation and acetylation of furfural on a Ru based catalyst. Theoretical calculations describing the adsorption and hydrogenation mechanism of furfural and 2, 5-hydroxymethylfurfural (HMF) on metals are scarce.[65] To the best of our knowledge, concerning Ru[66-68] and Ni,[69] only flat surfaces have been considered in theoretical studies. Yet, it has

been shown that co-adsorption of solvents,[70] ligands[71] and the presence of hydrides[70,72] onto metallic surfaces has a significant effect on the adsorption energies of catalytic substrates. To the best of our knowledge the theoretical work described here is the first study describing the catalytic reactivity of furfural and furfural derivative compounds on a Ru hydrogenated surface, modelled by a *hcp* Ru_{55} NP.

Experimental section

General Methods. All operations were carried out under argon atmosphere using standard Schlenk techniques or in an MBraun glovebox. Solvents were purified by standard methods or by an MBraun SPS-800 solvent purification system. [Ru(η^4-C_8H_{12})(η^6-C_8H_{10})] was purchased from Nanomeps Toulouse, [Ni(η^4-C_8H_{12})$_2$] from Strem Chemicals, polyvinylpyrrolidone (PVP), furfural (FF), tetrahydrofuran (THF), decane, and dodecane from Sigma-Aldrich, furfuryl alcohol (HF) and tetrahydrofurfuryl alcohol (HMTHF) from Alfa Aesar, CO and H_2 from Air Liquid. All these reactants were used as received. Metal content was established by inductively coupled plasma optical emission spectroscopy (ICP-OES) performed at the "Laboratoire de Chimie de Coordination, Toulouse" in a Thermo Scientific ICAP 6300 instrument. Liquid NMR measurements were performed on a Bruker Avance 300 or 400 instrument. Attenuated total reflection infrared (ATR-IR) spectra were recorded on a Perkin-Elmer GX2000 spectrometer available in a glovebox, in the range 4000-400 cm^{-1}. Transmission electron microscopy (TEM) and high resolution transmission electron microscopy (HRTEM) analyses were performed at the "Centre de microcaracterisation Raimond Castaing, UMS 3623, Toulouse" by using a JEOL JEM 1011 CXT electron microscope operating at 100 kV with a point resolution of 4.5 Å or a JEOL JEM 1400 operating at 120 kV with a point resolution of 2.0 Å. High resolution analyses were conducted using a JEOL JEM 2100F equipped with a Field Emission Gun (FEG) operating at 200 kV with a point resolution of 2.3 Å and a JEOL JEM-ARM200F Cold FEG operating at 200 kV with a point resolution of >1.9 Å. The approximation of the particles mean size was stablished through a manual analysis of enlarged micrographs by measuring at least 200 particles on a given grid. The magnetic hysteresis curves were acquired by using a MPMS 5 QUANTUM DESIGN Magnetometer (cryo-aimant 5T; cryostat 2 K-400 K) using a superconducting quantum interference device (SQUID). Wide angle X-ray scattering (WAXS) measurements were performed at CEMES on a diffractometer dedicated to pair distribution function (PDF) analysis: graphite-monochromatized molybdenum radiation (0.07169nm), solid-state detection and low background setup. Samples were sealed in Lindemann glass capillaries (diameter 1 mm) to avoid any oxidation after filling in a glove box. For all samples data were collected on an extended angular range (129 degrees in 2theta) with counting times of typically 150s for each of the 457 data points, thus allowing for PDF analysis. Classic corrections (polarization and absorption in cylindrical geometry) were applied before reduction and Fourier transform. X-ray photoelectron spectroscopy

(XPS) experiments under ultra high vacuum (UHV) were performed with Thermo Scientific K-Alpha apparatus using a monochromatised Al Kα (EAl Kα = 1486.6 eV) X-ray source. The X-ray spot size was about 400 µm. The Pass energy was fixed at 30 eV with a step of 0.1 eV for core levels and 160 eV for surveys (step 1eV). The spectrometer energy calibration was done using the Au 4f7/2 (83.9 ± 0.1 eV) and Cu 2p3/2 (932.8 ± 0.1 eV) photoelectron lines. XPS spectra were recorded in direct mode N (Ec) and the background signal was removed using the Shirley method. The flood Gun was used to neutralize charge effects on the top surface. Quantitative analyses of the catalytic reaction mixtures were performed via gas chromatography (GC) analyses using internal standard technique and solutions of commercially available products. GC analyses were performed on a SHIMADZU GC-2014 equipped with a SUPELCOWAX 10 capillary column (30 m x 0.25 mm x 0.25µm). The method used for furfural reaction mixture analyses consists on: carrier gas flow, He, 1.25 ml/min; injector temperature, 250 °C; detector (FID) temperature, 250 °C; oven program, 50 °C (hold 3 min) to 240 °C at 20 °C/min (hold 10 min) for a total run time of 22.5 min; retention time, dodecane, 6.8 min; furfural, 9.2 min; tetrahydrofurfuryl alcohol, 9.4 min; acetal, 10.0 min; furfuryl alcohol, 10.4 min; 2-propoxymethyl furan, 10.6 min; and 1,2-pentanediol, 11.1 min. GC-MS analyses were performed in a Shimadzu QP2010 Ultra GC-MS (EI mode), equipped with a ZEBRON ZB-5ms capillary column (30 m x 0.25 mm x 0.25µm). The method used for furfural reaction mixture analyses consists on: carrier gas flow, He, 1 ml/min; injector temperature, 250 °C; detector (FID) temperature, 250 °C; oven program, 40 °C (hold 0.5 min) to 250 °C at 20 °C/min (hold 10 min) for a total run time of 21 min; retention time: furfural, 3.6 min; furfuryl alcohol, 3.8 min; tetrahydrofurfuryl alcohol , 4.0 min; 1,2-pentanediol, 4.3 min; 2-propoxymethyl furan, 4.7 min; dodecane, 6.3 min; and acetal, 6.7 min.

Computational details. *DFT calculations of metal nanoclusters.* Software: Vienna ab initio simulation package, VASP;[73,74] spin polarized DFT; exchange-correlation potential approximated by the generalized gradient approach proposed by Perdew, Burke, and Ernzerhof (PBE);[75] projector augmented waves (PAW) full-potential reconstruction;[76,77] PAW data sets for Ru treating the (*n*-1)*p*, (*n*-1)*d* and *ns* states (*i.e*. 14 valence electrons); kinetic energy cutoff: 500 eV; Γ-centered calculations;[78] Gaussian smearing (σ) of 0.02 eV width, energies being therefore extrapolated for σ = 0.00 eV; geometry optimization threshold: residual forces on any direction less than 0.02 eV/Å; supercell size: 20×23×20 Å^3 (ensures a vacuum space of *ca*. 10 Å between periodic images of the nanoclusters).

Ru_{55} model. The model is an hcp spheroid. Its geometrical characteristics, as well as a hydride coverage study were previously published in ref.[79]. It has also been used to study the adsorption properties of phenylpyridine[80] and of ethanoic acid[81] at the surface of hydrogenated RuNPs.

Adsorption energies.

$$E_{\text{ads}}(\text{H}) = \frac{1}{n}\left[E\left(n\text{H}^{*}\right) - E(\text{NP}) - \frac{n}{2}E(\text{H}_2)\right]$$

$$E_{\text{ads}}(\text{L}) = \frac{1}{n}\left[E\left(n\text{L}^{*}\right) - E(\text{NP}) - nE(\text{L})\right]$$

i.e. in the case of hydrides it is a dissociative adsorption energy. *Charge calculations*. A Mulliken population analysis (MPA) from VASP wavefunction was performed by integrating up to the Fermi energy the density of states projected onto an atomic Slater basis set (pDOS). The projection of the PAW wavefunction was achieved with the Lobster software, using the pbeVASPfit basis set.[82] The charge spilling, a criterion that assesses the quality of the projection was systematically lower than 1.0%. A comparison of such MPA charges with other electronic density decomposition schemes (AIM-Bader, Natural Population Analyzis, CM5) can for example be found in ref.[83]. *d-band center values* (ε_d). They were calculated from the pDOS obtained with LOBSTER, see details in Ref.[84] The principle underlying this model[85] is that the binding energy of an adsorbate to a metal surface is largely dependent on the electronic structure of the surface itself. The closer is ε_d to the Fermi energy (E_F), the stronger the bonding on the surface. A large ($E_F - \varepsilon_d$) involves weak adsorption energies.

Synthesis of RuNi NP. In a typical experiment, [Ru(η^4-C_8H_{12})(η^6-C_8H_{10})] and/or [Ni(η^4-C_8H_{12})$_2$] complexes were introduced in a Fisher Porter bottle, together with PVP, and dissolved with THF in a glovebox. The yellow solution was pressurized with 3 bar of H_2 and heated to 85 °C. After some minutes, the solution turned black. The reaction was kept at this temperature overnight under vigorous stirring. After this period of time, the H_2 excess was removed and the colloidal suspension was concentrated under reduced pressure. Pentane was added to precipitate the NP. After filtration under argon with a cannula, the black solid powder was washed twice with pentane and filtered again before drying under reduced pressure overnight. For each metal ratio studied, the quantities of reactants are detailed hereafter.

Ru/PVP: 140.4 mg (0.445 mmol) of [Ru(η^4-C_8H_{12})(η^6-C_8H_{10})], 150 mg of PVP, and 40 mL of THF. Yield: 102.7 mg. ICP anal.: 24.2% Ru.

Ru_3Ni_1/PVP: 105.3 mg (0.334 mmol) of [Ru(η^4-C_8H_{12})(η^6-C_8H_{10})], 30.6 mg (0.111 mmol) of [Ni(η^4-C_8H_{12})$_2$], 150 mg of PVP, and 40 mL of THF. Yield: 131.2 mg. ICP anal.: 17.0% Ru; 3.7% Ni.

Ru_1Ni_1/PVP: 45.0 mg (0.143 mmol) of [Ru(η^4-C_8H_{12})(η^6-C_8H_{10})], 39.2 mg (0.143 mmol) of [Ni(η^4-C_8H_{12})$_2$], 100 mg of PVP, and 40 mL of THF. Yield: 72.3 mg. ICP anal.: 10.2% Ru; 5.7% Ni.

Ru_1Ni_3/PVP: 35.1 mg (0.111 mmol) of [Ru(η^4-C_8H_{12})(η^6-C_8H_{10})], 91.8 mg (0.334 mmol) of [Ni(η^4-C_8H_{12})$_2$], 150 mg of PVP, and 40 mL of THF. Yield: 147.8 mg. ICP anal.: 7.9% Ru; 14.6% Ni.

Ru_1Ni_{20}/PVP: 7.0 mg (0.022 mmol) of [Ru(η^4-C_8H_{12})(η^6-C_8H_{10})], 116.3 mg (0.423 mmol) of [Ni(η^4-C_8H_{12})$_2$], 150 mg of PVP, and 40 mL of THF. Yield: 92.9 mg. ICP anal.: 1.5% Ru; 17.6% Ni.
Ni/PVP: 117.6 mg (0.425 mmol) of [Ni(η^4-C_8H_{12})$_2$], 150 mg of PVP, and 40 mL of THF. Yield: 114.1 mg. ICP anal.: 17.9% Ni.

Surface Reactivity with CO. The adsorption of CO on the surface of the NP was performed in the solid state. A purified sample of NP was introduced in a Fischer-Porter bottle. The reactor was pressurized with 1.5 bar of CO for 24 h. Then, the CO gas was evacuated under reduced pressure for 20 min, and the ATR-IR spectra were recorded in a glovebox.

Catalytic hydrogenations. The hydrogenation of furfural was carried out in a 200 mL stainless steel high-pressure batch Top Industrie reactor. In a typical experiment, a mixture of the catalyst (0.02 mmol of metal), dodecane or decane (0.5 mmol) as internal standard, and furfural (4 mmol) as substrate in 15 mL of the desired solvent were loaded into the autoclave inside the glovebox. The autoclave was purged three times with H_2 to remove the inert atmosphere, heated to 125 °C, and charged with 20 bar of H_2. The stirring rate was fixed at 1200 rpm. Samples of the reaction mixture were taken at different time intervals and analysed by gas chromatography. Quantitative analyses of the reaction mixtures were performed via GC using calibration solutions of commercially available products. Hot filtration was performed following the same procedure described above using furfural in THF and Ru_1Ni_1/PVP as catalyst. The reaction was stopped after one hour of reaction. After the introduction of the reactor into the glovebox the catalyst was removed by filtration of the solution through an alumina path. The solution was introduced once more into the reactor, free of catalyst. Afterwards, the reactor was pressurized again to 20 bar of H_2, heated at 125°C, and allowed to react for one additional hour at a stirring rate of 1200 rpm. Finally, the solution was analysed by GC.

Results and discussion

Synthesis and characterization of metallic nanoparticles

Bimetallic NP were synthesized by decomposing [Ru(η^4-C_8H_{12})(η^6-C_8H_{10})] and [Ni(η^4-C_8H_{12})$_2$] complexes in the presence of PVP as stabilizer in THF at 85°C under 3 bar of H_2 pressure. Several Ru/Ni molar ratios were used for the synthesis of the bimetallic NP, ranging from 3 to 0.01, with the aim to obtain several compositions to control further the catalytic reactivity. Ru and Ni monometallic counterparts were also synthesised following the same procedure. Metal content of the synthesised nanomaterials was ascertained by ICP analyses (Table 1) and NP shape and size by TEM analyses (Table 1, Figure 1, and Figure S1-S7).

Table 1. Metal content and mean size of metal nanoparticles

NP	Ru content (%)[a]	Ni content (%)[a]	NP composition (from ICP)	Mean size (nm)[b]
Ru/PVP	24.2	-	Ru/PVP	1.0 ± 0.2
Ni/PVP	-	15.5	Ni/PVP	5.6 ± 1.2[c]
Ru_3Ni_1/PVP	17.0	3.7	$Ru_{2.7}Ni_{1.0}$/PVP	1.5 ± 0.3
Ru_1Ni_1/PVP	10.2	5.7	$Ru_{1.0}Ni_{1.0}$/PVP	1.5 ± 0.3
Ru_1Ni_3/PVP	7.9	14.6	$Ru_{1.0}Ni_{3.2}$/PVP	1.2 ± 0.2
Ru_1Ni_{20}/PVP	1.5	17.6	$Ru_{1.0}Ni_{20.0}$/PVP	1.4 ± 0.3

[a]ICP analysis. [b]Mean values of nanoparticle size determined from TEM images by considering at least 200 particles. [C]Tripodal shaped nanoparticles.

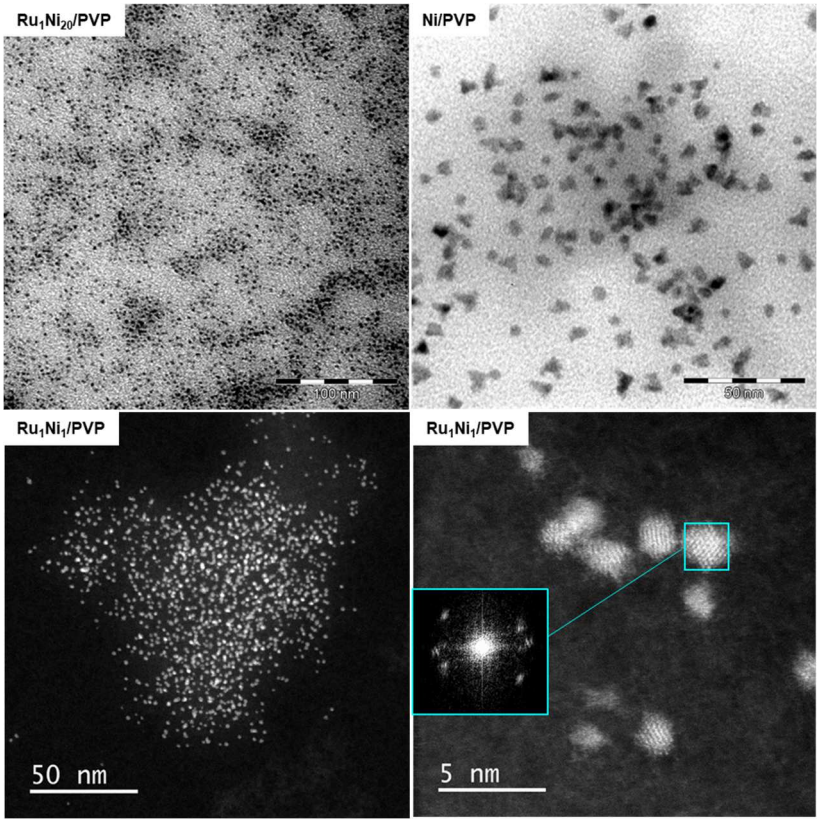

Figure 1. TEM images of Ru_1Ni_{20}/PVP (top left, scale bar = 100 nm); Ni/PVP (top right, scale bar = 50 nm); HAADF-STEM images of Ru_1Ni_1/PVP (bottom left, scale bar = 50 nm; bottom right scale bar = 5 nm, with FFT pattern as insert).

At 85°C $[Ni(\eta^4\text{-}C_8H_{12})_2]$ complex decomposed in the presence of H_2 and PVP giving a characteristic black suspension within minutes, in agreement with previous results published elsewhere.[86] In this case, shaped NP, mainly tripodal, were obtained displaying a mean size of 5.6 ± 1.2 nm. Likewise, Ru/PVP

was smoothly obtained from [Ru(η^4-C_8H_{12})(η^6-C_8H_{10})] at same reaction conditions giving rise to ultra-small Ru NP of 1.0 ± 0.2 nm. The Ru NP were similar in terms of size and shape than when synthesised at room temperature,[87] indicating a low impact of the synthetic temperature for the nucleation and growth of these Ru NP in THF. Bimetallic NP were also obtained straightforward from the simultaneous decomposition of [Ru(η^4-C_8H_{12})(η^6-C_8H_{10})] and [Ni(η^4-C_8H_{12})$_2$] at 85°C using different Ru/Ni ratios, leading to the formation of black suspensions within minutes from the initial bright yellow solutions. TEM analyses displayed in all cases spherical and small NP ranging from 1.2 to 1.5 nm, even at high Ni content (Figure 1, Table 1, and Figure S2-S5 and S7). This is in contrast with the monometallic Ni NP synthesised at the same reaction conditions, which led to larger and shaped NP, suggesting that Ru could act as a seed mediator to decompose more easily Ni complex generating ultra-small bimetallic NP. This evidence is in agreement with previous observations suggesting that Ru is able to reduce Ni^{2+} trough hydrogen spillover.[16,17] Fact which is supported by the different decomposition kinetics under H_2 observed for [Ni(η^4-C_8H_{12})$_2$] and [Ru(η^4-C_8H_{12})(η^6-C_8H_{10})], being faster the later. HRTEM analyses confirmed the bimetallic nature for Ru_1Ni_1/PVP (Figure 1, Figure S7). HAADF-STEM-EDX (high-angle annular dark field-scanning transmission electron-energy-dispersive X-ray spectroscopy) analyses in this sample showed that Ru and Ni coexist in the same NP (Figure S7). Lattices of bimetallic NP were analysed and indexed trough fast Fourier transformation (FFT) of the HAADF-STEM images. Reflections corresponding to 0.227, 0.209 and 0.199 nm were found which were attributed to slightly shorter Ru (100), (002), and (101) planes, in agreement with X-ray analyses. Further WAXS analyses revealed a complex situation however consistent with the formation of bimetallic NP. Clearly, the combination of two or more phases (including PVP) makes the extraction of structural information delicate, however some strong elements can be evidenced: specific patterns, especially in real space, and significant changes in the metallic bond-length. Ni/PVP sample (Figure 2) is fully consistent with bulk Ni (fcc). Similarly, Ru_1Ni_{20}/PVP is dominated by the *fcc* structure of metallic Ni however with a loss in crystallinity. At the other end of the composition range, the situation is different, Ru/PVP synthesized at 85°C has a distorted structure compared to the expected *hcp* structure observed for Ru/PVP materials synthesized at room temperature.[88] A specific pattern of this distorted structure can also be observed (0.2-0.5 nm range) for Ru_3Ni_1 and Ru_1Ni_1, with decreasing amplitude. This is consistent with a core-shell organization since for core-shell systems, the RDF has always been observed as dominated by the core's organization.[89,90] The decreasing amplitude of this pattern reflects the dilution by another contribution much less organized which cannot be clearly defined. Ru_1Ni_3/PVP is more complex, from the RDF it is much closer to the Mn-β organization often observed for very small metallic NP.[91-95] This sample exhibits an average bond length of 0.262nm intermediate between Ni and Ru ones, 0.250 and 0.268nm, respectively, suggesting an alloy, however Mn-β is not a compact structure which makes the exact chemical order an open question.

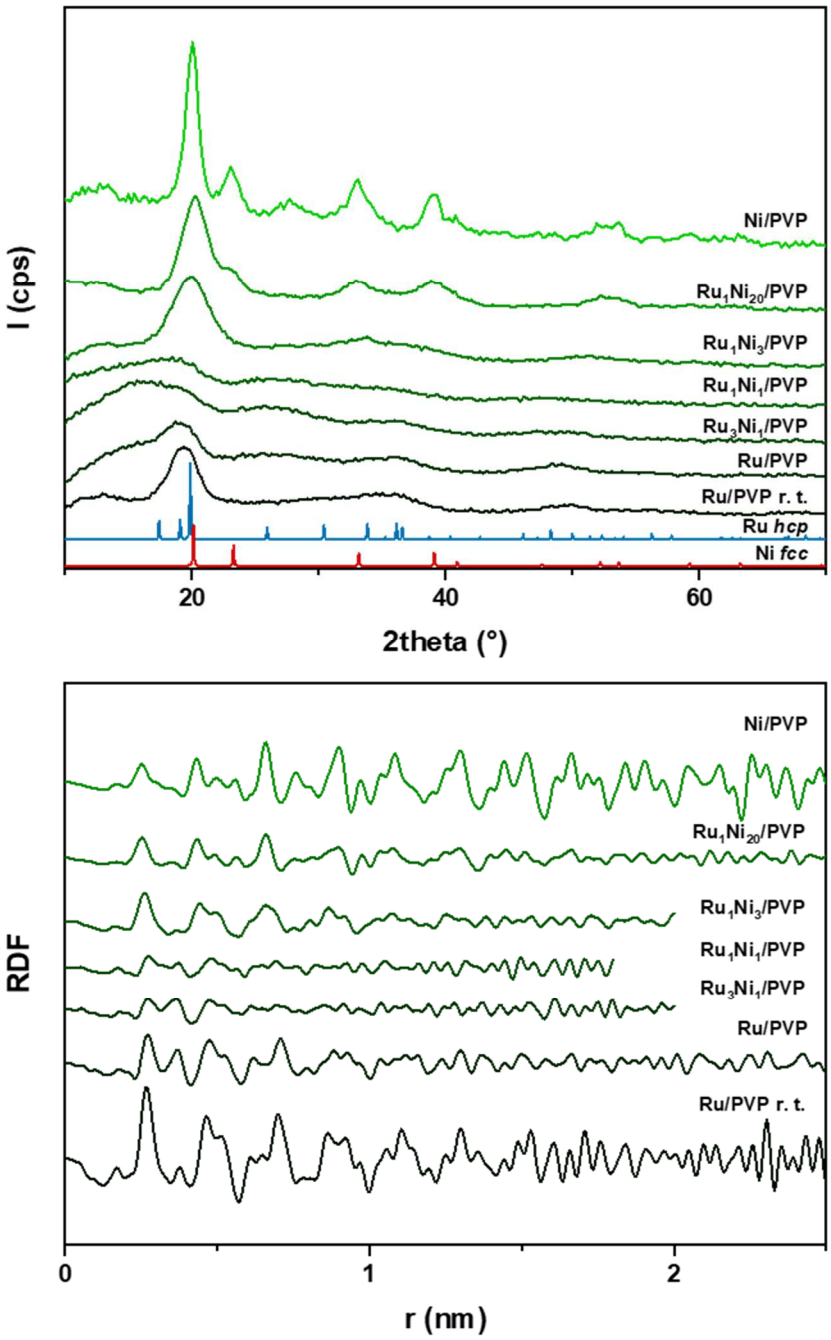

Figure 2. Diffractograms of RuNi/PVP, Ru/PVP, and Ni/PVP together with the reference of Ru *hcp* and Ni *fcc* structures (top); and related radial distribution functions (RDFs) (bottom).

Ex situ XPS under ultrahigh vacuum (UHV) analyses were performed on Ru_1Ni_1/PVP, Ru/PVP, Ni/PVP, and PVP. Survey spectra and high-resolution scan spectra together with the fitting peaks of the corresponding components are presented in Figure 3 and S8-S11, respectively, Table S1 summarizes binding energies together with the concentration of the fitted peaks in atomic %, of the four samples.

XPS spectrum of PVP (Figure S11) is closely with what is expected for this compound. Ru_1Ni_1/PVP, Ru/PVP, and Ni/PVP showed similar spectra of that described for PVP (Figure S8, S9 and S10, respectively). The peaks corresponding to Ru and Ni were in general lower in intensity of what it was expected from their composition, which is attributed to PVP probably embedded efficiently the metallic nanoparticles. In this context, the fitting of the peaks is less accurate and it is difficult to estimate the binding energies shifts and to relate them to structural features, in addition, the samples were exposed briefly to air before analysis, which partially oxi(hydroxi)dized the metals. Nevertheless, comparing both monometallic samples to the bimetallic Ru_1Ni_1/PVP shows that, concerning Ru, Ru $3d_{5/2}$ have slightly higher binding energies in the bimetallic sample, 279.7 eV vs 279.5 eV. The Ni $2p_{3/2}$ signal of Ni/PVP and Ru_1Ni_1/PVP showed different chemical environments. The Ni $2p_{3/2}$ signal at higher binding energy, around 855 eV, corresponding to an oxi(hydroxi)dation of the top surface. The other $Ni2p_{3/2}$ response at 852.5 eV and 852.3 eV indicate the presente of Ni metal, in respectively bimetallic and monometallic environments. Due to the low intensity of the Ru and Ni signals it is difficult to confirm any charge transfer between both metals and the direction of it, but the change on binding energies can be tentatively attributed to the close vicinity to Ru and Ni in the bimetallic sample.

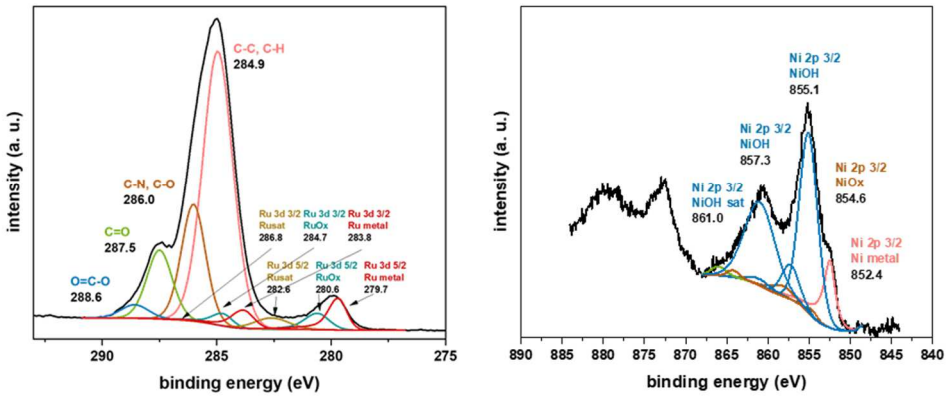

Figure 3. High-resolution XPS spectra of Ru_1Ni_1/PVP; left, C 1S and Ru 3d; right, Ni 2p.

ATR-FTIR spectra of the mono- and bimetallic NP were recorded in a glovebox. Infrared spectra are displayed in Figure S12, in which only frequencies attributed to the stabilizing polymer were observed. CO is a vibrational probe, which can give valuable information about the surface of metal NP.[96] Lower energies of the vCO band indicate more electron density on the metal centres; by comparison of the CO frequencies it is possible to determine the effect of a ligand in a given metallic surface[87,97] or to identify the chemical order in bimetallic NP.[63,98,99] With this aim, bimetallic and monometallic nanocatalysts were exposed to CO in the solid state and the respective IR spectra are depicted in Figure S13. CO band was clearly observed on the IR spectrum of Ru/PVP, measured at wavelength of 2010 cm^{-1}. The same peak was also observed on Ru_3Ni_1/PVP and Ru_1Ni_1/PVP, although the intensity was

distinctly reduced. On samples with high Ni content only peaks attributed to the PVP were observed, which was assigned to the plausible formation of $[Ni(CO)_4]$, only observable at low temperature measurements in solid state due to its volatility.[100] The lack of CO band in Ru_1Ni_3/PVP and Ru_1Ni_{20}/PVP probably indicates that Ru metal is not accessible to the CO atmosphere, suggesting that only Ni is on the surface of the NP in agreement with a core-shell structure. Taking into account the size of the nanoparticles and the metallic content ascertained by ICP analyses, the percentage of coverage of the nanoparticle surface with Ni is estimated to be ≈45% for Ru_3Ni_1/PVP and ≈77% for Ru_1Ni_1/PVP, while Ru_1Ni_3/PVP should present a complete shell of Ni (Table S2). This estimation is in line with the observation and intensity of CO band on the IR spectra, but also with some catalytic results, which are discussed below.

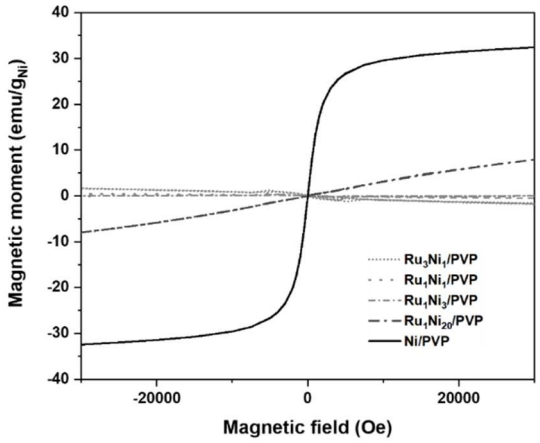

Figure 4. Magnetic hysteresis cycles of bimetallic and monometallic nanoparticles measured at room temperature.

The magnetic curves of bimetallic NP measured at room temperature, and corrected of diamagnetic PVP are presented in Figure 4. High Ru content samples, *i. e*. Ru_3Ni_1/PVP, Ru_1Ni_1/PVP, and Ru_1Ni_3/PVP, display a curve typical of diamagnetic materials, while Ru_1Ni_{20}/PVP with high Ni content and a particle size of 1.4 ± 0.3 nm is paramagnetic. These results are in line with previous observations, in which magnetization abruptly decreases by the addition of smalls amounts of Ru onto Ni.[101,102] Ni/PVP which is composed of tripodal shaped nanoparticles of 5.5 ± 1.2 nm of size showed a ferromagnetic behaviour with a magnetic saturation (Ms) value of 32.4 emu/g_{Ni}. The Ms is NP size-dependent for Ni NP,[103] explaining the low Ms observed in Ni/PVP sample, compared to bulk Ni (M_S = 54.4 emu/g_{Ni}).[104] Nevertheless, it can not be discarded that small amounts of oxidized Ni surface could also contribute to the loss of magnetic moment.

Catalytic activity of RuNi nanoparticles on the selective furfural hydrogenation

The catalytic performances of RuNi nanoparticles were investigated in the selective furfural hydrogenation (Scheme 1) at 125°C, a constant pressure of 20 bar of H_2, and a magnetic stirring set up at 1200 rpm, which should discard mass transfer limitations. Solvent effects, as well as the impact of the nanoparticle composition are analysed thereafter. Results are summarized in Tables 2 and 3. Time-concentration curves are presented in the SI, Figure S14 and S15. Using THF as solvent led to the selective hydrogenation of the aldehyde moiety of furfural (FF) to produce the alcohol, 2-(hydroxymethyl)furan (HF) or furfuryl alcohol, in very high selectivities in all cases. Increasing the Ni content partially promoted the total hydrogenation of furfural towards tetrahydrofurfuryl alcohol (HMTHF) in THF (Table 2). Ru/PVP nanocatalyst displayed the best performances if both activity and selectivity are considered, reaching full conversion in less than 24h with high selectivity towards the alcohol (up to 99%). This result is in agreement with previous works,[105,106] in which HF was obtained in high percentage (up to 96%) using PVP stabilizedRu NP at 30°C, even though it is worth noting that in our experimental conditions, *i. e.* higher reaction temperature (125°C), Ru/PVP was completely selective towards the hydrogenation of the aldehyde moiety. In order to understand this high selectivity an experiment was set up using furfuryl alcohol as substrate and employing the same reaction conditions. Time-concentration curve presented in the Figure S17 (left) shows distinctly that the reduction reaction of the heteroaromatic ring proceeds but it is disfavoured (TOF = 22 h^{-1}) compared to the hydrogenation of the aldehyde (TOF = 51 h^{-1}) in the same reaction conditions, which points out to a weaker adsorption of HF with respect to the aldehyde compound towards the nanocatalyst surface. Theoretical calculations show that the coordination of the C=O bond, in η^1(O) or η^2(C=O) coordination mode, towards the hydrogenated ruthenium surface is favoured against other coordination modes investigated (see theoretical calculation discussion for more details). These results are in line with the fact that the aldehyde is first hydrogenated. As the coordination of the aromatic ring into the Ru metallic surface seems disfavoured with respect other possible coordination of substrates and products in THF, it could be the reason why the heteroaromatic ring is sluggishly reduced under the reaction conditions used here.

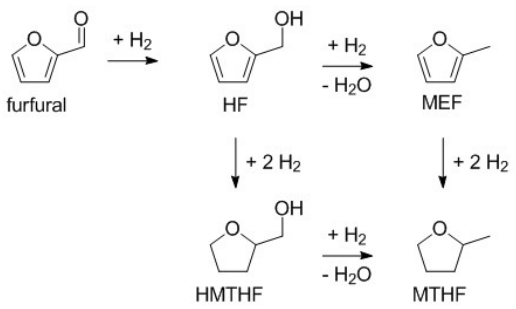

Scheme 1. Simplified reaction scheme of the selective catalytic hydrogenation of furfural into various valuable products. Furfural (FF), 2-(hydroxymethyl)furan (HF), tetrahydrofurfuryl alcohol (HMTHF), 2-methylfuran (MEF), and 2-methyltetrahydrofuran (MTHF).

Concerning the RuNi NP a volcano shape tendency is observed for activity, in which the maximum is centered on the Ru_1Ni_1/PVP sample (Figure 5), which points to a synergistic effect between both metals. Ni/PVP was very slow in comparison to the other nanocatalysts of the series probably due to the size and shape of the NP. Of all catalysts tested, monometallic Ni showed the lowest selectivity towards furfuryl alcohol, as the fully hydrogenated product was produced from the beginning of the reaction (Figure S15 for time-concentration curve). Besides the effect of the bimetallic composition it is worth noting that the selectivity of the reaction was size-sensitive, Ru_1Ni_{20}/PVP with a size of 1.4 ± 0.3 nm and a high Ni content, displayed a selectivity towards HF of 94% at ca. 50 of conversion (Table 2, entry 19), while Ni/PVP displayed a selectivity towards HF of 72% at ca. 50% of conversion (Table 2, entry 24). If this size effect on selectivity was further confirmed, it could be an interesting approach to obtain products as 2-methylfuran (MEF) from furfural or 2,5-dimethylfuran (DMF) from 2, 5-hydroxymethylfurfural (HMF), as this result points to the direction in which ultra-small nanoparticles are less prone to hydrogenate the aromatic ring. NP size effects on catalysis are well-known.[107,108] For furfural hydrogenation size effects have been described.[109] Specifically, for the hydrogenation of the C=O moiety of furfural, size effects have been observed for Pt NP[110] and Cu nanowires,[111] but did not concern the hydrogenation of the aromatic ring. On the other hand, the reduction of HF towards HMTHF was found to be structure-sensitive using a series of Ni/SiO_2 catalyst displaying a mean size from 2.6 to 12.8 nm; smaller TOFs values were observed in larger NP, implying that the hydrogenation of the heteroaromatic ring was favoured in smaller NP.[112]

Table 2. Selective hydrogenation of furfural in THF using Ru, Ni and RuNi nanocatalysts.[a]

Entry	Catalyst	TOF (h^{-1})[b, c]	Time (h)	Conversion (%)[c]	HF (%)[c]	HMTHF (%)[c]
1	Ru/PVP	51	1	20	>99	<1
2			5	51	>99	<1
3			24	98	>99	<1
4			29	100	>99	<1
5	Ru_3Ni_1/PVP	52	1	16	98	2
6			5	33	98	2
7			24	93	98	2
8			29	98	92	8
9	Ru_1Ni_1/PVP	62	1	20	95	5
10			5	42	96	4
11			24	79	97	3

12			29	84	97	3
13	Ru_1Ni_3/PVP	51	1	18	92	8
14			5	42	93	7
15			24	85	94	6
16			29	89	94	6
17	Ru_1Ni_{20}/PVP	38	1	11	89	11
18			5	26	92	8
19			24	57	94	6
20			29	63	93	7
21	Ni/PVP	18[d]	1	9	79	21
22			5	24	84	16
23			24	44	85	15
24			29	49	72	27

[a]Reaction conditions: 2×10^{-2} mmol of metal, 4 mmol of furfural, 0.5 mmol of decane (internal standard), 20 bar of H_2, 125°C, 15 mL of THF. [b]TOFs calculated at 1 h of reaction according to the surface amount of metal. [c]Determined by GC using an internal standard technique. [d]TOF calculated at 1 h of reaction according to the total amount of metal.

A different scenario is observed when 1-propanol is used as solvent in the hydrogenation reaction. Results are summarized in Table 3. TOFs are significantly higher than in THF, which at first was attributed that 1-propanol solubilizes slightly better H_2 than THF.[113-115] Nevertheless, the formation of acetal in Ru surfaces, together with the observation that the solvent effect depends on the composition of the NP, pointed out to a different reason. DFT calculations on $Ru_{55}H_{70}$ covered with several molecules of THF and 1-propanol show that the adsorption energies per solvent, d-band center values of surface and core Ru atoms, and average charges of hydrides and metal atoms are very similar in both configurations (Figure S30), discarding thus any influence of the solvent in terms of promoting any change in the electronic configuration of the Ru surfaces. For that reason, we further explored the reaction pathway theoretically, which is discussed below. It emerges from the calculations that the adsorption of the C=O bond of FF, in η^1(O) or η^2(C=O) coordination modes, denoted as σ-FF* and π-FF* in Figure 7 and 10, respectively, onto the Ru hydrogenated surfaces is more favourable in the case in which propanolates are co-adsorbed in the surface. Thus, pointing to higher activities for propanolated-modified surfaces as observed experimentally.

The TOG displayed by Ru_1Ni_{20}/PVP was increased approximately three times in 1-propanol with respect to THFand for the other Ni containing catalysts the TOF was roughly increased twice (Figure 5). The beneficial effect of the alcoholic solvent on the activity was less pronounced in Ru/PVP nanocatalyst, which increased the activity of a factor of 1.5. Ru/PVP was very active for the formation of acetal at the early stages of the reaction, which could be detrimental for the hydrogenation reaction. The acetal formation is observed in significant amounts when using high loaded Ru nanocatalysts (Ru/PVP, Ru_3Ni_1/PVP, and Ru_1Ni_1/PVP), bu it is supressed using Ru_1Ni_3/PVP and Ru_1Ni_{20}/PVP, in which Ni atoms are exclusively at the surface (see Table S2). A good correlation is found between the quantity of acetal

synthesised and the percentage of Ru on the surface (see Table S2). Ru/PVP produced 1.5 mmol of acetal, while Ru_3Ni_1/PVP, and Ru_1Ni_1/PVP produced 0.5 and 0.3 mmol, respectively, which fits better with the amount of Ru atoms at the surface (57% and 23%, respectively), than with the total amount of Ru on the sample. Additionally, this reactivity could tentatively be attributed to electronic effects, as Ru/PVP, which is a Ru electron-deficient nanocatalysts,[87] promotes the acetalisation reaction.[116,117] Introducing Ni to the nanocatalysis should increase the Ru electron density,[11] supressing or disfavouring this reaction, as it was observed here.

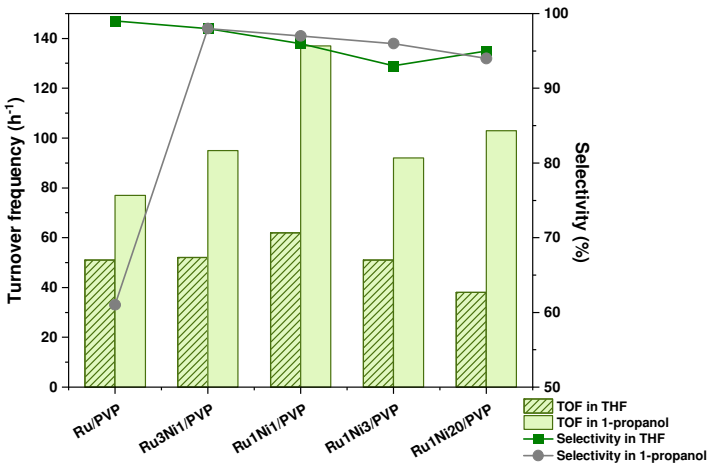

Figure 5. Turnover frequency (bars) and selectivity towards 2-(hydroxymethyl)furan (dots) as function of catalysts in the selective hydrogenation of furfural in THF (dashed bars, square dots) and 1-propanol (green bars, circle dots).

Table 3. Selective hydrogenation of furfural in 1-propanol using Ru, Ni and RuNi nanocatalysts.[a]

Entry	Catalyst	TOF (h^{-1})[b, c]	Time (h)	Conversion (%)[c]	HF (%)[c]	HMTHF (%)[c]	Acetal (%)[c, d]
1	Ru/PVP	104 (77)	1	39	50	1	49
2			5	90	67	1	32
3			24	>99	51	18	28[e]
4			29	>99	41	26	28[e]
5	Ru_3Ni_1/PVP	110 (95)	1	34	83	2	15
6			5	71	81	2	17
7			24	>99	82	2	15
8			29	>99	78	2	19
9	Ru_1Ni_1/PVP	149 (137)	1	47	92	3	5
10			5	81	90	3	8
11			24	>99	89	3	8
12			29	>99	90	3	7
13	Ru_1Ni_3/PVP	110 (92)	1	40	95	4	1
14			5	71	94	4	2
15			24	96	93	4	3
16			29	97	93	4	3
17	Ru_1Ni_{20}/PVP	103 (103)	1	30	93	7	-

18			5	57	94	6	-
19			24	87	94	6	-
20			29	90	94	6	-
21	Ni/PVP	31[f]	1	15	99	1	-
22			5	43	88	6	6
23			24	88	83	5	12
24			29	93	83	5	12

[a]Reaction conditions: 2×10^{-2} mmol of metal, 4 mmol of furfural, 0.5 mmol of decane (internal standard), 20 bar of H_2, 125°C, 15 mL of 1-propanol. [b]TOFs calculated at 1 h of reaction according to the surface amount of metal; in brackets: TOFs of hydrogenation reaction. [c]Determined by GC using an internal standard technique. [d]Determined by GC-MS.[e]1,2 pentanediol also detected. [f]TOF calculated at 1 h of reaction according to the total amount of metal.

Besides the formation of acetal, which is prejudicial in general terms for the selectivity of the reduction reaction, 1-propanol affected also the selectivity. Ru/PVP is able to hydrogenate the heteroaromatic moiety in 1-propanol while this reactivity is highly impeded in THF. From a theoretical point of view the adsorption of the heteroaromatic ring seems less favourable in THF than in 1-propanol, which is discussed below. In an independent catalytic test furfuryl alcohol was hydrogenated by Ru/PVP using the same reaction conditions, time-concentration curves are presented in Figure S16. The aromatic ring was hydrogenated efficiently with a TOF = $79h^{-1}$, which is similar to the one observed for the hydrogenation of the aldehyde, TOF = $77h^{-1}$, pointing out to similar affinity for the metallic surface. This value is in contrast with the low TOF displayed in THF, $22h^{-1}$. Interestingly, the hydrogenolysis of the C-O bond of the ring was observed in this case, and 1, 2-pentanediol was obtained in a 27% selectivity; which is similar to the reactivity described for Ru-Mn,[118] Ru/MnO_x[119] and Ru/Al_2O_3.[120]

The addition of Ni to the surface of the NP hampered the hydrogenation of the aromatic ring (Table 3, entries 3 and 4 vs. entries 7 and 8). A good compromise in terms of activity and selectivity was found for Ru_1Ni_1/PVP nanocatalyst, in which aside from presenting the highest TOF of the series, the fully hydrogenated and the acetal products formation is almost supressed. It is also noteworthy that Ru_1Ni_{20}/PVP displayed very interesting catalytic properties in regards with the high amount of first row metal contained in its formulation.

After catalysis all nanocatalysts were analysed by TEM. Also, the catalytic solutions were filtered through an alumina path, evaporated to dryness and analysed by ICP. ICP analyses on samples from catalysis carried out in THF pointed out that no leaching is occurring; on the other hand, on samples from catalysis carried out in 1-propanol, Ru and Ni were detected, nevertheless, always under the detection limit, except for nanocatalysts Ru_1Ni_{20}/PVP, which the ICP quantification represents approximately 15% of catalyst leaching. We attributed this behaviour to the high solubility of PVP in 1-

propanol, which is detrimental for a good catalyst separation. Indeed, our tentatives to recycle the catalysts were unfruitful as the separation of the catalysts was arduous in both solvents. Hot filtration experiment, *i. e.* the catalysts filtered off from the reaction mixture at 1h of reaction and the filtrate reengaged in catalysis under same reaction conditions, did not produce any additional product, proving the heterogeneous nature of the catalyst. Details are given in the experimental part and in Figure S17. Further, the TEM analyses after catalysis show no significant change in size or shape for most of the catalysts (Table S3, Figures S18-S29), except for Ru_1Ni_{20}/PVP, in which size evolved significantly together with a broadening of the size distribution in the samples analysed after the catalysis performed in 1-propanol. This is in line with the leaching detected for this particular sample, which could indicate that the Ru_1Ni_{20}/PVP catalysts is not stable under this specific reactions conditions, leading to the lixiviation of Ni atoms which may cause Ostwald ripening of the NP increasing further their size. Similarly, Ni/PVP size and shape evolved during catalysts, even if more robust as leaching was not detected. Both Ni/PVP and Ru_1Ni_{20}/PVP size changes and leaching for the later, indicate that the presence of Ru is stabilizing Ni atoms onto the NP surface, which can be an advantage as Ni based catalysis is prone to leaching issues in liquid-phase hydrogenation.[121]

Theoretical calculations

As previously discussed, the hydrogenation of furfural catalysed by the Ru/PVP nanocatalyst has been carried out either in THF or in 1-propanol, the nature of the solvent influencing the outcome of the catalytic reaction. In THF, the Ru/PVP nanocatalyst converts furfural selectively toward the corresponding alcohol, HF, with a full conversion in 24 h. In 1-propanol, on the other hand, the Ru/PVP nanocatalyst is faster but less selective, converting, in only 5h, 90% of the furfural to both the corresponding HF and the furfuryl acetal species. In the presence of 1-propanol, in addition, the formation of the fully hydrogenated HMTHF compound, containing a hydrogenated hydrofuran cycle, has been also observed for longer reaction times. In order to check whether the slower activity observed in THF could be ascribed to the stronger absorption of THF on the nanoparticle surface with respect to 1-propanol, we compared the adsorption energy of two molecules of THF and 1-propanol, respectively, on a $Ru_{55}H_{70}$ nanoparticle. $Ru_{55}H_{70}$ is a good descriptor of the Ru/PVP nanocatalyst under hydrogenation conditions.[79] First, in terms of size, Ru/PVP is 1.1 ± 0.2 nm in size and $Ru_{55}H_{70}$ about 1 nm. Second, in terms of hydride coverage, $Ru_{55}H_{70}$ displaying a hydride coverage of 1.7 H/Ru_{surf}, which is likely to be the coverage under hydrogenation conditions.[79] Furfural hydrogenation has been theoretically studied before involving Ru based catalysts.[66-68] As shown in Figure S31, interestingly, the average adsorption energy of 10 THF or 10 PrOH molecules is almost identical (-*ca*. -8 $kcal.mol^{-1}$). Given that the coordination of 10 additional hydrides on the same sites is not competitive (Eads: -4.1 $kcal.mol^{-1}$), this value of *ca.* -8 $kcal.mol^{-1}$ is sufficiently large, at this hydride coverage, to consider that THF and

1-propanol can adsorb on the nanoparticule surface. The similar adsorption energies computed for the two solvents, moreover, suggest that the different FF conversion rate observed in the two solvent media is not related to the different accessibility of the nanoparticle sites but rather to the involvement of two different mechanistic patways in THF and in 1-propanol, respectively. Our calculations also show that the conversion of all 10 adsorbed propanol molecules into the corresponding propanolate and hydride species is not favourable (see Figure S32). However, the dissociative adsorption of a few amount of 1-propanol molecules is a favourable process, thus indicating that adsorbed propanolates behave as transient species to be accounted for in the reaction mechanisms. Finally, electron charges and d-band center values are also given in Figure S31. Adsorbed 1-propanol or THF species do not significantly change the d-band center of the surface Ru atoms, in line with the weak σ-donor character of these species. In other words, in contrast to strongly bound ligands or hydrides, these solvent molecules adsorbed on the surface are not expected to significantly influence the catalytic activity of the metal atoms on the surface.

We therefore decided to investigate some possible reaction intermediates involved in the hydrogenation mechanisms in the two different reaction media, THF or 1-propanol. As stated before, it will be carried out on an hydrogenated 1nm RuNP, $Ru_{55}H_{70}$. Compared to the bare surfaces, this model accounts for a possible modulation of the reactivity by surface hydrides.[122] But their mobility makes uneasy the identification of stationary points along a reaction pathway. In other words, achieving a full and relevant mechanistic study of the hydrogenation reaction of furfural on small Ru NP is challenging, and out of the scope of the present study.[123] As some of us has recently reported in the case of carboxylic acids, the O-H activation by the Ru NP surface is however supposed to be easy.[81,97,124] A recent investigation of the H/D exchange at the carbon alpha of differently substituted amines also shown that C-H bond activation and formation are favourable processes at the Ru NP surface.[125,126] We will only consider in the following sections adsorption energies of reactants, products and reaction intermediates, barrier heights being assumed low to moderate. The hydrogenation mechanism involved in the two different reaction media, THF or 1-propanol, was investigated on two different models: the $Ru_{55}H_{70}$ cluster, and its counterpart with two propanol molecules lying in the neighbourhood of the considered active site (see Figure 6). In both cases, we chose the same site (highlighted in yellow in Figure 6), at the interface between the (001) and (101) facets of the Ru NP. While reactions (1) and (2) may occur in acidic media, it is interesting to underline that the surface hydrogen species involved in the present Ru NP-catalyzed hydrogenation process, are hydrides (atomic charges are given in Figure S33).

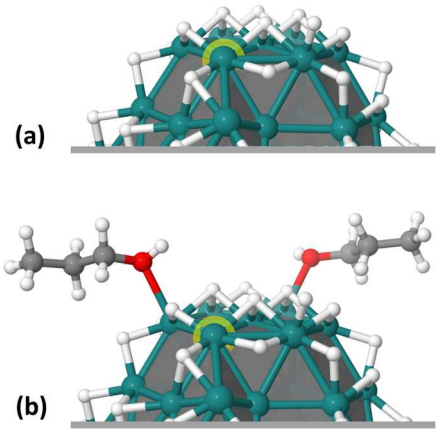

Figure 6. $Ru_{55}H_{70}$ models used to investigate the hydrogenation reactions (a) in THF and (b) in 1-propanol. The considered active site is highlighted with a yellow halo. The lower part of the models is not shown for the sake of clarity.

Prior to the description of the found reaction pathways, we shall first give some energy clues regarding the hydrogenation reactions at the chosen DFT level of theory:

(1) FF + H_2 → HF

(2) HF + $2H_2$ → HMTHF

(3) HMTHF + H_2 → 1,2-PeD

(4) FF + 2PrOH → acetal + H_2O

Reactions (1), (2) and (3) are exothermic by -18.0 kcal.mol^{-1}, -44.3 kcal.mol^{-1} and -26.7 kcal.mol^{-1}, respectively. Reaction (4), known to occur in alcoholic solvents,[116] is exothermic by only -6.5 kcal.mol^{-1}. Although being exothermic, the hydrogenation is an uneasy process from a kinetic point of view. This is why hydrogenated Ru NP are interesting all-in-one catalysts, which offer several and versatile active sites, while favouring barrierless H_2 dissociative chemisorption at their surface. The resulting hydrides are very mobile on the metal surface and they can be coordinated either top, edge-bridging or face-capping, as evidenced by both NMR experiments[127] and DFT calculations.[128] It is noteworthy that the aforementioned energy values are the same for the homologous catalytic reactions occurring at the active sites (*) of the Ru NP:

(1') FF + H_2 + 2* → HF + 2*

(2') HF + $2H_2$ + 3* → HMTHF + 3*

(3') HMTHF + H_2 + 2* → 1,2-PeD + 2*

(4') FF + 2PrOH + 3* → acetal + H_2O + 3*

where 2* and 3*, for example, mean that two and three different Ru NP sites are involved in the reaction. Mind that an active site can either be a single surface Ru atom, a bimetallic edge or a higher μ_n index coordination site.

Hydrogenation in THF. A possible underlying mechanism of (1') in THF is shown in Figure 7. THF and FF can both adsorb on the considered active site of $Ru_{55}H_{70}$ by their σ-donating oxygen atom, at the advantage of FF (-12.0 kcal.mol^{-1} *vs*. -10.6 kcal.mol^{-1}). After adsorption of FF, a π coordination of the carbonyl function may probably favour the first transfer of a hydride from the surface to the carbonyl carbon of the FF* molecule. The resulting intermediate, σ-HF_{CH}*$Ru_{55}H_{69}$, that lies at -13.1 kcal.mol^{-1}, exhibits a bridging bidentate oxygen atom. The alternative mechanism involving the transfer of a hydride from the surface to the carbonyl oxygen function of the FF* molecule is also accessible, affording a slightly less stable intermediate (π-HF_{OH}*$Ru_{55}H_{69}$: -12.3 kcal.mol^{-1}). The following transfer of a second hydride from the surface to either the furfuryl alcoholate oxygen or the furfuryl carbon atom may then occur, providing the corresponding furfuryl alcohol (HF*) adsorbed on the resulting $Ru_{55}H_{68}$ nanoparticle by both the lone pair of the alcohol function and a π interaction between the furanyl moiety and the metal surface (-11.6 kcal.mol^{-1}). With a desorption energy of 20.5 kcal.mol^{-1}, the release of the HF molecule from the $Ru_{55}H_{68}$ surface is unlikely at mild temperature. However, under H_2 pressure, the initial $Ru_{55}H_{70}$ surface is then regenerated, allowing the release of HF by a thermodynamically favourable process of -18.0 kcal.mol^{-1}.

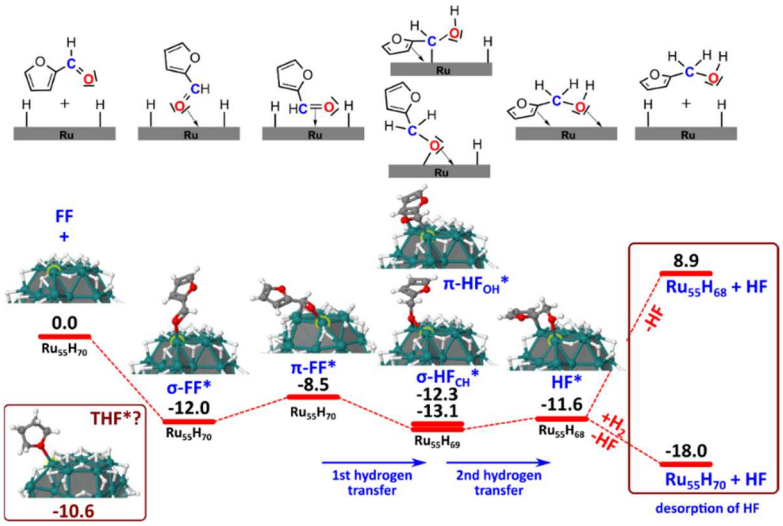

Figure 7. Energy profile for the FF hydrogenation on a $Ru_{55}H_{70}$ nanoparticle (reaction 1') in THF. Energies are given in kcal.mol^{-1}.

The feasibility of reaction (2') to occur in THF, which experimentally appeared to be highly disfavoured, is next investigated. Given that the Ru NP surface is the sole source of hydrogen, the formation of HMTHF should involve a stable π coordination of FF or HF on the Ru NP. We have checked the π coordination of the furanyl cycle on several sites, but at such high H-coverage adsorption energies are too weak to allow this coordination mode (Figure S34). The only noticeable exception is the special atom of this $Ru_{55}H_{70}$ model that mimics a small step together with the active site considered all throughout this study. The π coordination of the HF furanyl cycle on these two Ru sites, indeed, is stable by -26.9 kcal.mol^{-1}, resulting thus more favourable than the HF desorption (Figure 8). Such μ-η^2:η^2 coordination, however, involves two metal sites and if we compare this π adsorption mode of HF with the co-adsorption of 1 THF and 1 HF molecules on the same metal sites, we obtain an exothermicity of -34.7 kcal.mol^{-1}, suggesting that the alternative THF coordination hampers the π coordination of HF and therefore the consequent formation of HMTHF.

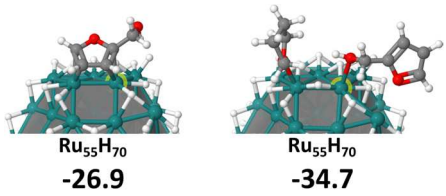

Figure 8. Possible species involved in the HF furanyl cycle hydrogenation, following reaction (2'). Energies are given in kcal.mol^{-1}.

Hydrogenation in 1-propanol. While in THF, the hydrogens needed to hydrogenate the carbonyl function of the aldehyde must necessarily come from the hydrides absorbed on the Ru nanoparticle, in 1-propanol, they may also derive from the hydrogen of the 1-propanol alcohol function. As shown in Figure 9, interestingly, the propanol molecules may either interact with the absorbed FF* compound by outer-sphere H interactions, or adsorb on the surface via their OH groups. The adsorption of the 1-propanol molecules on the $Ru_{55}H_{70}$ nanoparticle is more stable by 10 kcal.mol^{-1} than the formation of two H-bond interactions with the absorbed FF* species, indicating that any involvement of propanol on the hydrogenation mechanism occurs after its adsorption on the $Ru_{55}H_{70}$ nanoparticle.

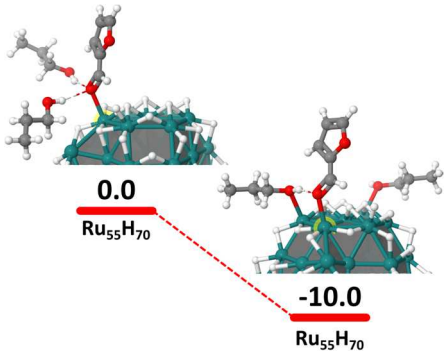

Figure 9. Favourable adsorption of two 1-propanol molecules on a $Ru_{55}H_{70}$ nanoparticle. Energies are given in kcal.mol^{-1}.

If we consider now the reaction in 1-propanol, the two hydrogens needed to reduce the aldehyde function can derive i) from the hydrogens absorbed on the $Ru_{55}H_{70}$ nanoparticle surface, leading to the same profile discussed above for THF; ii) from the 1-propanol OH functions, after adsorption of the propanol molecules on the $Ru_{55}H_{70}$ nanoparticle surface and iii) from both the $Ru_{55}H_{70}$ nanoparticle surface and the 1-propanol OH functions.

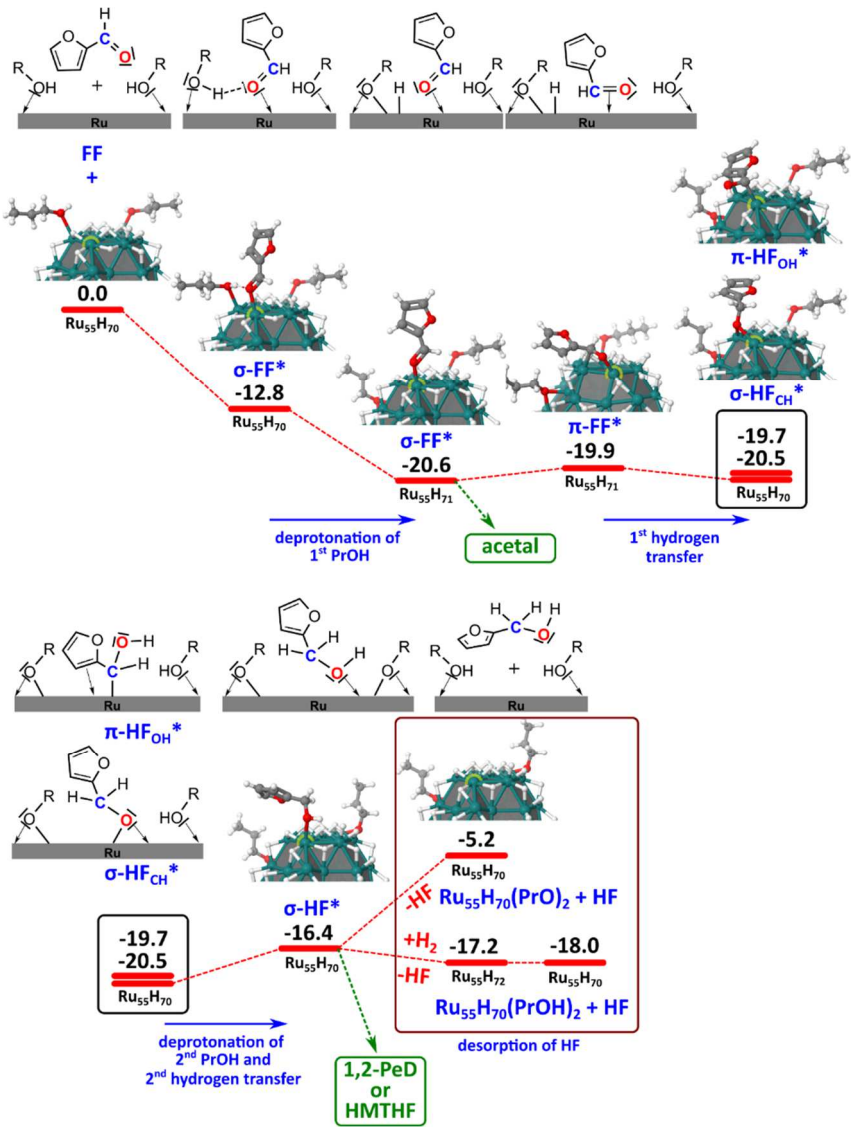

Figure 10. A possible energy profile for the FF hydrogenation on a $Ru_{55}H_{70}$ nanoparticle (reaction 1') in 1-propanol. Possible starting points toward the formation of acetal, HMTHF or 1,2-pentanediol (1,2-PeD) are also shown (see text and Figures 11 and 12). Energies are given in kcal.mol^{-1}.

Taking as starting catalyst the $Ru_{55}H_{70}$ nanoparticle with two absorbed 1-propanol molecules, the first step involves the adsorption of the FF molecule (σ-FF*$Ru_{55}H_{70}$: -12.8 kcal.mol^{-1}), followed by the O-H bond dissociation on the surface of one of the two absorbed propanol molecules (σ-FF*$Ru_{55}H_{71}$: -20.6 kcal.mol^{-1}), as shown in Figure 10. The first hydride transfer from the Ru surface to the carbonyl carbon of the FF aldehyde function may then occur, providing the furfuryl alcoholate molecule (-20.5 kcal.mol^{-1}), monocoordinated to the Ru surface via the alcoholate oxygen atom in a bidentate mode. Also in this case, as previously seen for the THF case, the alternative mechanism involving the transfer of an hydride from the Ru surface to the carbonyl oxygen function of the FF* molecule is also accessible, affording a slightly less stable intermediate (π-HF_{OH}*$Ru_{55}H_{70}$: -19.7 kcal.mol^{-1}). The second hydrogenation process may then occur involving either the proton transfer from the second absorbed 1-propanol molecule to the furfuryl alcoholate oxygen, or the hydride transfer from the Ru surface to the furfuryl carbon atom. Both pathways afford the same furfuryl alcohol product (HF*), adsorbed on the $Ru_{55}H_{70}$ nanoparticle through its OH group (σ-HF*$Ru_{55}H_{70}$: -16.4 kcal.mol^{-1}). Under H_2 pressure, the two 1-propanolate molecules are protonated, regenerating the initial catalyst after desorption of the furfuryl alcohol. In order to draw the whole reaction pattern observed in 1-propanol, we also investigated the mechanism involved in the formation of the furfuryl acetal derivative, as reported in Table 3. Once again we only localised the possible intermediates, assuming that the barrier heights are low to moderate. Reaction intermediates that could possibly pave the acetal formation are reported in Figure 11.

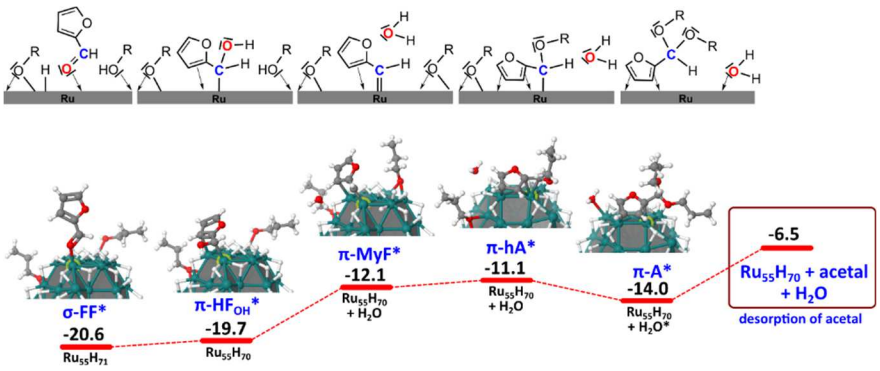

Figure 11. Energy clues on a possible reaction pathway for the formation of acetal (reaction 4') in 1-propanol, starting from the σ-FF intermediate reported in Figure 10. Energies are given in kcal.mol^{-1}.

Starting from the $Ru_{55}H_{70}$ nanoparticle with two absorbed 1-propanol molecules, the first part of the mechanism is identical to that previously reported for the FF hydrogenation, involving the adsorption of the FF molecule (-12.8 kcal.mol^{-1}, σ-FF*$Ru_{55}H_{70}$ in Figure 10), followed by the O-H bond dissociation on the surface of one of the two absorbed propanol molecules (σ-FF*$Ru_{55}H_{71}$: -20.6 kcal.mol^{-1}). The transfer of a hydride from the Ru surface to the carbonyl oxygen of the FF* molecule may then occur, providing a furfuryl alcohol species which is bonded to the Ru surface through the carbonyl carbon

atom (π-HF_{OH}*$Ru_{55}H_{70}$: -19.7 kcal.mol^{-1}). The transfer of a hydrogen atom either from the propanol or from the Ru surface may then lead to the protonation of the furfuryl hydroxo group followed by the release of one water molecule. This provides the concomitant formation of a relatively stable intermediate (π-MyF*$Ru_{55}H_{70}$: -12.1 kcal.mol^{-1}), displaying a sp^2 hybridized C atom strongly bonded to the Ru surface (selected geometry parameters and charges of this surprising dimetallacycle intermediate are compared in Figure S34 to π-HF_{OH}*$Ru_{55}H_{70}$). The consecutive attack of one and then two alcoholate molecules on the furfuryl carbon atom bonded to the Ru surface may finally yield the monoether and diether (acetal) derivatives, lying respectively at -11.1 and -14.0 kcal.mol^{-1}.

Let us now consider the possible hydrogenation of the furanyl moiety, with a possible 1,2-diol formation consecutive to a ring-opening reaction.[119] Again, only thermodynamics will be considered, the calculation of kinetic parameters being well beyond the scope of this theoretical contribution. We shall just conjecture that (i) hydrogenated Ru NP are good hydrogenation catalysts,[10] (ii) the hydrogenation of furanyl involves its preliminary π coordination on the metal surface, (iii) a ring-opening reaction is easier from tetrahydrofurfuryl alcohol than from the unsaturated furfuryl alcohol. It is at the basis of the reaction pathway exploration reported in Figure 12. The π coordination of HF involves an extra stabilization by 9 kcal.mol^{-1} with respect to σ-HF*. Then, the hydrogenation of the cycle counterbalances the Ru-H bond-breaking. With a concomitant dissociative adsorption of three H_2 molecules and the possible regeneration of adsorbed propanol molecules, the final release of HMTF (reaction 2') is exothermic by -65.5 kcal.mol^{-1}. Provided that the ring-opening barrier height is low enough, σ-HMTF* can also lead to 1,2-pentanediol, which desorption is exothermic by -92.2 kcal.mol^{-1} (reaction 3'). Such energy could falsely be interpreted as a strong thermodynamic driving force, whereas in reality kinetics make uneasy such transformations. Notwithstanding a π coordination of HF (π-HF* intermediate) stronger than the σ counterpart – but not too strong by virtue of the Sabatier principle − and that no solvent molecules or other intermediates compete on the same active sites.

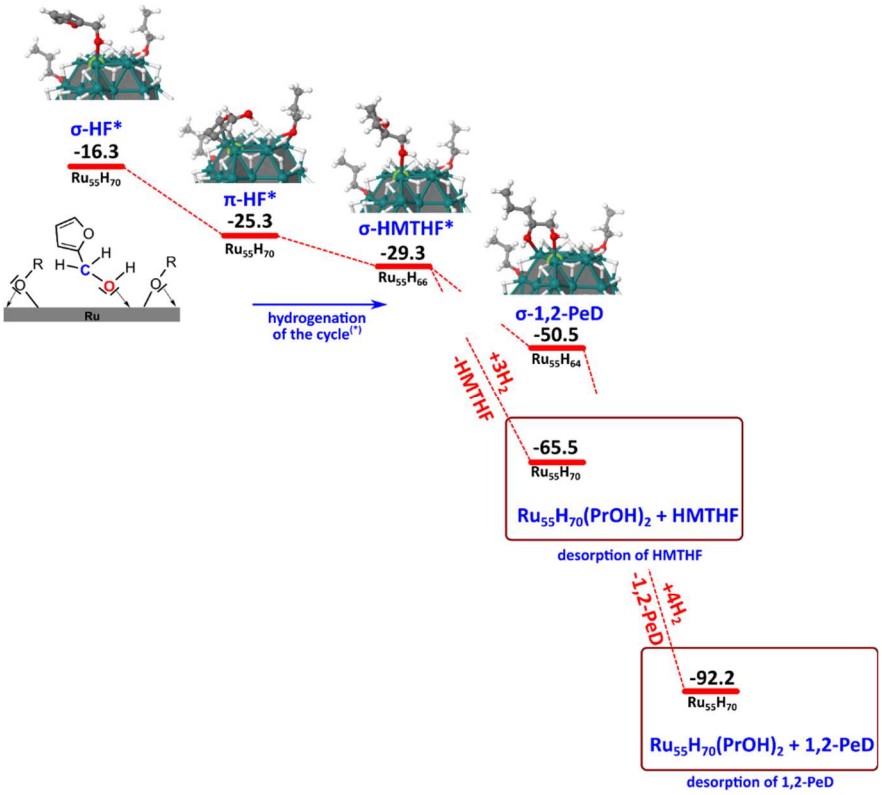

Figure 12. Possible reaction pathways for the formation of HMTHF (reaction 2') and 1,2-pentanediol (1,2-PeD, reaction 3'), in 1-propanol. They both originate from the σ-FF intermediate reported in Figure DFT5. (*): the four activated hydrides ongoing from π-HF to σ-HMTHF were randomly removed from the surface. Energies are given in kcal.mol^{-1}.

Conclusions

Nanometric-sized RuNi bimetallic particles have been successfully prepared from organometallic complexes and PVP as stabilizer, in one-pot conditions. These RuNi nanoparticles display a segregated structure in which Ni is located onto the surface. By controlling the ratio of both metals, it was possible to obtain different Ni coverages while maintaining similar nanoparticle sizes, ranging from 1.2 to 1.7 nm. This could be achieved by taking benefit of the different reduction kinetics of the two metal precursors, which favoured a seed-mediated growth and thus the formation of segregated nanoparticles versus alloyed nanoparticles. These RuNi nanoparticles were proven efficient catalysts for the selective hydrogenation of furfural and compared to monometallic counterparts. A volcano shape trend was found for different RuNi compositions in terms of activity, pointing out to a synergy between both metals. RuNi nanoparticles with a Ru/Ni ratio of 1 displayed the highest TOF (149 h^{-1}) using 1-propanol as solvent. Pure Ru catalyst was the most selective catalyst in THF, with a selectivity towards furfuryl alcohol of over 99%. In 1-propanol, RuNi nanoparticles with high Ni content (Ni/Ru >1) displayed selectivities higher that 90% towards furfuryl alcohol at full conversion. The RuNi nanocatalysts were found robust in the catalysis conditions applied. Moreover, if the monometallic Ni

and high Ni content RuNi nanoparticles appeared prone to leaching, the presence of Ru seems to stabilize the Ni present on the NP surface . We have relied in DFT calculations to obtain some insights about the coordination mode and adsorption strength of the species present during catalysis using a similar in size model of hydrogenated Ru nanoparticles. To our knowledge, this is the first time that such RuNi systems have been studied for the hydrogenation of furfural. Altogether, theoretical and experimental results fit well to explain activity and selectivity trends observed with the series of RuNi catalysts here studied.

Acknowledgements

This work was supported by the CNRS, which we gratefully acknowledge. The authors acknowledge the financial support from Ministère de l'Enseignement supérieur, de la Recherche et de l'Innovation for M. C. grant. R. Castaing characterization platform in Toulouse is also acknowledged.

References

(1) Sankar, M.; Dimitratos, N.; Miedziak, P. J.; Wells, P. P.; Kiely, C. J.; Hutchings, G. J. Designing bimetallic catalysts for a green and sustainable future. *Chem. Soc. Rev.* **2012**, *41*, 8099-8139.

(2) Kang, X.; Li, Y.; Zhu, M.; Jin, R. Atomically precise alloy nanoclusters: syntheses, structures, and properties. *Chem. Soc. Rev.* **2020**, *49*, 6443-6514.

(3) Luneau, M.; Lim, J. S.; Patel, D. A.; Sykes, E. C. H.; Friend, C. M.; Sautet, P. Guidelines to achieving high selectivity for the hydrogenation of α,β-unsaturated aldehydes with bimetallic and dilute alloy catalysts: a review. *Chem. Rev.* **2020**, *120*, 12834–12872.

(4) Gilroy, K. D.; Ruditskiy, A.; Peng, H.-C.; Qin, D.; Xia, Y. Bimetallic nanocrystals: syntheses, properties, and applications. *Chem. Rev.* **2016**, *116*, 10414-10472.

(5) Bing, Y.; Liu, H.; Zhang, L.; Ghosh, D.; Zhang, J. Nanostructured Pt-alloy electrocatalysts for PEM fuel cell oxygen reduction reaction. *Chem. Soc. Rev.* **2010**, *39*, 2184-2202.

(6) Fang, H.; Yang, J.; Wen, M.; Wu, Q. Nanoalloy materials for chemical catalysis. *Adv. Mater.* **2018**, *30*, 1705698.

(7) Over, H. Surface chemistry of ruthenium dioxide in heterogeneous catalysis and electrocatalysis: from fundamental to applied research. *Chem. Rev.* **2012**, *112*, 3356-3426.

(8) Hinrichsen, O.; Rosowski, F.; Muhler, M.; Ertl, G. The microkinetics of ammonia synthesis catalyzed by cesium-promoted supported ruthenium. *Chem. Eng. Sci.* **1996**, *51*, 1683-1690.

(9) Muhler, M.; Rosowski, F.; Hinrichsen, O.; Hornung, A.; Ertl, G.; Hightower, J. W.; Nicholas Delgass, W.; Iglesia, E.; Bell, A. T.: Ruthenium as catalyst for ammonia synthesis. In *Studies in Surface Science and Catalysis*; Elsevier, 1996; Vol. 101; pp 317-326.

(10) Axet, M. R.; Philippot, K. Catalysis with colloidal ruthenium nanoparticles. *Chem. Rev.* **2020**, *120*, 1085-1145.

(11) Li, M.; Wang, H.; Zhu, W.; Li, W.; Wang, C.; Lu, X. RuNi nanoparticles embedded in N-doped carbon nanofibers as a robust bifunctional catalyst for efficient overall water splitting. *Adv. Sci.* **2020**, *7*, 1901833pp.

(12) Zhu, L.; Sun, H.; Fu, H.; Zheng, J.; Zhang, N.; Li, Y.; Chen, B. H. Effect of ruthenium nickel bimetallic composition on the catalytic performance for benzene hydrogenation to cyclohexane. *Appl. Catal., A* **2015**, *499*, 124-132.

(13) Zhang, P.-F.; Zhang, J.-Y.; Sheng, T.; Lu, Y.-Q.; Yin, Z.-W.; Li, Y.-Y.; Peng, X.-X.; Zhou, Y.; Li, J.-T.; Wu, Y.-J.; Lin, J.-X.; Xu, B.-B.; Qu, X.-M.; Huang, L.; Sun, S.-G. Synergetic effect of Ru and NiO in

the electrocatalytic decomposition of Li_2CO_3 to enhance the performance of a Li-CO_2/O_2 battery. *ACS Catal.* **2020**, *10*, 1640-1651.

(14) Luo, Z.; Zheng, Z.; Li, L.; Cui, Y.-T.; Zhao, C. Bimetallic Ru-Ni catalyzed aqueous-phase guaiacol hydrogenolysis at low H_2 pressures. *ACS Catal.* **2017**, *7*, 8304-8313.

(15) Hu, Y.; Jiang, G.; Xu, G.; Mu, X. Hydrogenolysis of lignin model compounds into aromatics with bimetallic Ru-Ni supported onto nitrogen-doped activated carbon catalyst. *Mol. Catal.* **2018**, *445*, 316-326.

(16) Valdes-Martinez, O. U.; Suarez-Toriello, V. A.; de los Reyes, J. A.; Pawelec, B.; Fierro, J. L. G. Support effect and metals interactions for NiRu/Al_2O_3, TiO_2 and ZrO_2 catalysts in the hydrodeoxygenation of phenol. *Catal. Today* **2017**, *296*, 219-227.

(17) Tada, S.; Kikuchi, R.; Wada, K.; Osada, K.; Akiyama, K.; Satokawa, S.; Kawashima, Y. Long-term durability of Ni/TiO_2 and Ru-Ni/TiO_2 catalysts for selective CO methanation. *J. Power Sources* **2014**, *264*, 59-66.

(18) Chen, G.; Desinan, S.; Rosei, R.; Rosei, F.; Ma, D. Synthesis of Ni-Ru alloy nanoparticles and their high catalytic activity in dehydrogenation of ammonia borane. *Chem. - Eur. J.* **2012**, *18*, 7925-7930, S7925/7921-S7925/7926.

(19) Yang, Y.; Gao, G.; Zhang, X.; Li, F. Facile fabrication of composition-tuned Ru-Ni bimetallics in ordered mesoporous carbon for levulinic acid hydrogenation. *ACS Catal.* **2014**, *4*, 1419-1425.

(20) Zhang, J.; Teo, J.; Chen, X.; Asakura, H.; Tanaka, T.; Teramura, K.; Yan, N. A series of NiM (M = Ru, Rh, and Pd) bimetallic catalysts for effective lignin hydrogenolysis in water. *ACS Catal.* **2014**, *4*, 1574-1583.

(21) Qadir, M. I.; Bernardi, F.; Scholten, J. D.; Baptista, D. L.; Dupont, J. Synergistic CO_2 hydrogenation over bimetallic Ru/Ni nanoparticles in ionic liquids. *Appl. Catal., B* **2019**, *252*, 10-17.

(22) Chen, A.; Miyao, T.; Higashiyama, K.; Yamashita, H.; Watanabe, M. High catalytic performance of ruthenium-doped mesoporous nickel-aluminum oxides for Selective CO methanation. *Angew. Chem., Int. Ed.* **2010**, *49*, 9895-9898.

(23) Tada, S.; Kikuchi, R.; Takagaki, A.; Sugawara, T.; Oyama, S. T.; Urasaki, K.; Satokawa, S. Study of RuNi/TiO_2 catalysts for selective CO methanation. *Appl. Catal., B* **2013**, *140-141*, 258-264.

(24) Li, S.; Gong, D.; Tang, H.; Ma, Z.; Liu, Z.-T.; Liu, Y. Preparation of bimetallic Ni@Ru nanoparticles supported on SiO_2 and their catalytic performance for CO methanation. *Chem. Eng. J.* **2018**, *334*, 2167-2178.

(25) Ping, D.; Zhao, H.; Dong, X. Ni-doped TiO_2 nanotubes supported Ru catalysts for CO selective methanation in H_2-rich reformate gases. *React. Kinet., Mech. Catal.* **2018**, *124*, 619-631.

(26) Shang, X.; Deng, D.; Wang, X.; Xuan, W.; Zou, X.; Ding, W.; Lu, X. Enhanced low-temperature activity for CO_2 methanation over Ru doped Ni/$Ce_xZr_{(1-x)}O_2$ catalysts prepared by one-pot hydrolysis method. *Int. J. Hydrogen Energy* **2018**, *43*, 7179-7189.

(27) Ping, D.; Dong, X.; Zang, Y.; Feng, X. Highly efficient Ru/TiO_2-NiAl mixed oxide catalysts for CO selective methanation in hydrogen-rich gas. *Int. J. Energy Res.* **2017**, *41*, 2308-2317.

(28) Wang, C.; Ping, D.; Dong, X.; Dong, Y.; Zang, Y. Construction of Ru/Ni-Al-oxide/Ni-foam monolithic catalyst for deep-removing CO in hydrogen-rich gas via selective methanation. *Fuel Process. Technol.* **2016**, *148*, 367-371.

(29) Mohaideen, K. K.; Kim, W.; Koo, K. Y.; Yoon, W. L. Highly dispersed Ni particles on Ru/NiAl catalyst derived from layered double hydroxide for selective CO methanation. *Catal. Commun.* **2015**, *60*, 8-13.

(30) Zhen, W.; Li, B.; Lu, G.; Ma, J. Enhancing catalytic activity and stability for CO_2 methanation on Ni-Ru/γ-Al_2O_3 via modulating impregnation sequence and controlling surface active species. *RSC Adv.* **2014**, *4*, 16472-16479.

(31) Tada, S.; Minori, D.; Otsuka, F.; Kikuchi, R.; Osada, K.; Akiyama, K.; Satokawa, S. Effect of Ru and Ni ratio on selective CO methanation over Ru-Ni/TiO_2. *Fuel* **2014**, *129*, 219-224.

(32) Wang, S.; Vorotnikov, V.; Vlachos, D. G. Coverage-induced conformational effects on activity and selectivity: hydrogenation and decarbonylation of furfural on Pd(111). *ACS Catal.* **2015**, *5*, 104-112.

(33) Das, P. C.; Pradhan, N. C.; Dalai, A. K.; Bakhshi, N. N. Carbon monoxide hydrogenation over various titania-supported Ru-Ni bimetallic catalysts. *Fuel Process. Technol.* **2004**, *85*, 1487-1501.

(34) Crisafulli, C.; Scire, S.; Maggiore, R.; Minico, S.; Galvagno, S. CO_2 reforming of methane over Ni-Ru and Ni-Pd bimetallic catalysts. *Catal. Lett.* **1999**, *59*, 21-26.

(35) Crisafulli, C.; Scire, S.; Minico, S.; Solarino, L. Ni-Ru bimetallic catalysts for the CO_2 reforming of methane. *Appl. Catal., A* **2002**, *225*, 1-9.

(36) Li, D.; Atake, I.; Shishido, T.; Oumi, Y.; Sano, T.; Takehira, K. Self-regenerative activity of Ni/Mg(Al)O catalysts with trace Ru during daily start-up and shut-down operation of CH_4 steam reforming. *J. Catal.* **2007**, *250*, 299-312.

(37) Alvarez M, A.; Centeno, M. A.; Odriozola, J. A. Ru-Ni catalyst in the combined dry-steam reforming of methane: the importance in the metal order addition. *Top. Catal.* **2016**, *59*, 303-313.

(38) M, A. A.; Bobadilla, L. F.; Garcilaso, V.; Centeno, M. A.; Odriozola, J. A. CO_2 reforming of methane over Ni-Ru supported catalysts: On the nature of active sites by operando DRIFTS study. *J. CO_2 Util.* **2018**, *24*, 509-515.

(39) Jeong, J. H.; Lee, J. W.; Seo, D. J.; Seo, Y.; Yoon, W. L.; Lee, D. K.; Kim, D. H. Ru-doped Ni catalysts effective for the steam reforming of methane without the pre-reduction treatment with H_2. *Appl. Catal., A* **2006**, *302*, 151-156.

(40) Kodama, T.; Moriyama, T.; Shimoyama, T.; Gokon, N.; Andou, H.; Satou, N. Ru/Ni-Mg-O catalyzed SiC-foam absorber for solar reforming receiver-reactor. *J. Sol. Energy Eng.* **2006**, *128*, 318-325.

(41) Miyata, T.; Shiraga, M.; Li, D.; Atake, I.; Shishido, T.; Oumi, Y.; Sano, T.; Takehira, K. Promoting effect of Ru on Ni/Mg(Al)O catalysts in DSS-like operation of methane steam reforming. *Catal. Commun.* **2007**, *8*, 447-451.

(42) Wysocka, I.; Hupka, J.; Rogala, A. Catalytic activity of nickel and ruthenium-nickel catalysts supported on SiO_2, ZrO_2, Al_2O_3,and $MgAl_2O_4$ in a dry reforming process. *Catalysts* **2019**, *9*, 540.

(43) Chen, X.; Yan, N. Novel catalytic systems to convert chitin and lignin into valuable chemicals. *Catal. Surv. Asia* **2014**, *18*, 164-176.

(44) Bulut, S.; Siankevich, S.; van Muyden, A. P.; Alexander, D. T. L.; Savoglidis, G.; Zhang, J.; Hatzimanikatis, V.; Yan, N.; Dyson, P. J. Efficient cleavage of aryl ether C-O linkages by Rh-Ni and Ru-Ni nanoscale catalysts operating in water. *Chem. Sci.* **2018**, *9*, 5530-5535.

(45) Chen, G.; Desinan, S.; Nechache, R.; Rosei, R.; Rosei, F.; Ma, D. Bifunctional catalytic/magnetic Ni@Ru core-shell nanoparticles. *Chem. Commun.* **2011**, *47*, 6308-6310.

(46) Cao, N.; Su, J.; Luo, W.; Cheng, G. Hydrolytic dehydrogenation of ammonia borane and methylamine borane catalyzed by graphene supported Ru@Ni core-shell nanoparticles. *Int. J. Hydrogen Energy* **2014**, *39*, 426-435.

(47) Cao, N.; Su, J.; Hong, X.; Luo, W.; Cheng, G. In situ facile synthesis of Ru-based core-shell nanoparticles supported on carbon black and their high catalytic activity in the dehydrogenation of amine-boranes. *Chem. - Asian J.* **2014**, *9*, 562-571.

(48) Li, X.; Zeng, C.; Fan, G. Ultrafast hydrogen generation from the hydrolysis of ammonia borane catalyzed by highly efficient bimetallic RuNi nanoparticles stabilized on $Ti_3C_2X_2$ (X = OH and/or F). *Int. J. Hydrogen Energy* **2015**, *40*, 3883-3891.

(49) Roy, S.; Pachfule, P.; Xu, Q. High catalytic performance of MIL-101-immobilized NiRu alloy nanoparticles towards the hydrolytic dehydrogenation of ammonia borane. *Eur. J. Inorg. Chem.* **2016**, *2016*, 4353-4357.

(50) Umegaki, T.; Yabuuchi, K.; Yoshida, N.; Xu, Q.; Kojima, Y. In situ synthesized hollow spheres of a silica-ruthenium-nickel composite catalyst for the hydrolytic dehydrogenation of ammonia borane. *New J. Chem.* **2020**, *44*, 450-455.

(51) Li, L.-J.; Yi, W.-J.; Liu, T.-W.; Huang, C.; Chao, Z.-S. Hydrogenation of 3-hydroxypropanal into 1,3-propanediol over bimetallic Ru-Ni catalyst. *RSC Adv.* **2017**, *7*, 32027-32037.

(52) Braos-Garcia, P.; Garcia-Sancho, C.; Infantes-Molina, A.; Rodriguez-Castellon, E.; Jimenez-Lopez, A. Bimetallic Ru/Ni supported catalysts for the gas phase hydrogenation of acetonitrile. *Appl. Catal., A* **2010**, *381*, 132-144.

(53) Masalska, A. Properties and activities of ZSM-5 + Al_2O_3 supported RuNi catalysts in 1-methylnaphthalene hydrogenation: effect of Ru precursors. *Catal. Today* **2011**, *176*, 258-262.

(54) Mishra, D. K.; Lee, J.-M.; Chang, J.-S.; Hwang, J.-S. Liquid phase hydrogenation of D-glucose to D-sorbitol over the catalyst (Ru/NiO-TiO_2) of ruthenium on a NiO-modified TiO_2 support. *Catal. Today* **2012**, *185*, 104-108.

(55) Yadav, M.; Mishra, D. K.; Hwang, J.-S. Catalytic hydrogenation of xylose to xylitol using ruthenium catalyst on NiO modified TiO_2 support. *Appl. Catal., A* **2012**, *425-426*, 110-116.

(56) Mishra, D. K.; Hwang, J.-S. Selective hydrogenation of D-mannose to D-mannitol using NiO-modified TiO2 (NiO-TiO_2) supported ruthenium catalyst. *Appl. Catal., A* **2013**, *453*, 13-19.

(57) Zhu, L.; Cao, M.; Li, L.; Sun, H.; Tang, Y.; Zhang, N.; Zheng, J.; Zhou, H.; Li, Y.; Yang, L.; Zhong, C.-J.; Chen, B. H. Synthesis of different ruthenium nickel bimetallic nanostructures and an investigation of the structure-activity relationship for benzene hydrogenation to cyclohexane. *ChemCatChem* **2014**, *6*, 2039-2046.

(58) Zhu, L.; Cui, J.; Zhang, H.; Ruan, L.; Ma, N.; Zou, L.; Deng, T.; Chen, B. H.; Xiao, Q. Room-temperature morphology-controlled synthesis of nickel and catalytic properties of corresponding Ru/Ni catalysts. *ChemCatChem* **2019**, *11*, 3109-3116.

(59) Yang, J.; Shao, Q.; Huang, B.; Sun, M.; Huang, X. pH-Universal water splitting catalyst: Ru-Ni nanosheet assemblies. *iScience* **2019**, *11*, 492-504.

(60) Xia, J.; Volokh, M.; Peng, G.; Fu, Y.; Wang, X.; Shalom, M. Low-cost porous ruthenium layer deposited on nickel foam as a highly active universal-pH electrocatalyst for the hydrogen evolution reaction. *ChemSusChem* **2019**, *12*, 2780-2787.

(61) Wang, F.; Luo, Y.; Wang, Y.; Zhu, H. The preparation and performance of a novel spherical spider web-like structure Ru-Ni/Ni foam catalyst for $NaBH_4$ methanolysis. *Int. J. Hydrogen Energy* **2019**, *44*, 13185-13194.

(62) Amiens, C.; Ciuculescu-Pradines, D.; Philippot, K. Controlled metal nanostructures: fertile ground for coordination chemists. *Coord. Chem. Rev.* **2016**, *308*, 409-432.

(63) Qi, X.; Axet, M. R.; Philippot, K.; Lecante, P.; Serp, P. Seed-mediated synthesis of bimetallic ruthenium-platinum nanoparticles efficient in cinnamaldehyde selective hydrogenation. *Dalton Transactions* **2014**, *43*, 9283-9295.

(64) Braga, A. H.; Costa, N. J. S.; Philippot, K.; Goncalves, R. V.; Szanyi, J.; Rossi, L. M. Structure and activity of supported bimetallic NiPd nanoparticles: influence of preparation method on CO_2 reduction. *ChemCatChem* **2020**, *12*, 2967-2976.

(65) Chen, S.; Wojcieszak, R.; Dumeignil, F.; Marceau, E.; Royer, S. How catalysts and experimental conditions determine the selective hydroconversion of furfural and 5-hydroxymethylfurfural. *Chem. Rev.* **2018**, *118*, 11023-11117.

(66) Banerjee, A.; Mushrif, S. H. Reaction pathways for the deoxygenation of biomass-pyrolysis-derived bio-oil on Ru: a DFT study using furfural as a model compound. *ChemCatChem* **2017**, *9*, 2828-2838.

(67) Sampath, A.; Chang, S. A.; Flaherty, D. W. Catalytic hydrogen transfer and decarbonylation of aromatic aldehydes on Ru and Ru phosphide model catalysts. *J. Phys. Chem. C* **2018**, *122*, 23600-23609.

(68) Dong, H.; Zheng, Y.; Hu, P. A DFT study of direct furfural conversion to 2-methylfuran on the Ru/Co_3O_4 surface. *Phys. Chem. Chem. Phys.* **2019**, *21*, 1597-1605.

(69) Ren, G.; Wang, G.; Mei, H.; Xu, Y.; Huang, L. A theoretical insight into furfural conversion catalyzed on the Ni(111) surface. *Phys. Chem. Chem. Phys.* **2019**, *21*, 23685-23696.

(70) Shangguan, J.; Hensley, A. J. R.; Gradiski, M. V.; Pfriem, N.; McEwen, J.-S.; Morris, R. H.; Chin, Y.-H. C. The role of protons and hydrides in the catalytic hydrogenolysis of guaiacol at the ruthenium nanoparticle-water interface. *ACS Catal.* **2020**, *10*, 12310-12332.

(71) Luo, Z.; Min, Y.; Nechiyil, D.; Bacsa, W.; Tison, Y.; Martinez, H.; Lecante, P.; Gerber, I. C.; Serp, P.; Axet, M. R. Chemoselective reduction of quinoline over Rh-C_{60} nanocatalysts. *Catal. Sci. Technol.* **2019**, *9*, 6884-6898.

(72) Leng, F.; Gerber, I. C.; Lecante, P.; Moldovan, S.; Girleanu, M.; Axet, M. R.; Serp, P. Controlled and chemoselective hydrogenation of nitrobenzene over Ru@C_{60} catalysts. *ACS Catal.* **2016**, *6*, 6018-6024.

(73) Kresse, G.; Furthmüller, J. Efficient iterative schemes for *ab initio* total-energy calculations using a plane-wave basis set. *Phys. Rev. B* **1996**, *54*, 11169-11186.

(74) Kresse, G.; Furthmüller, J. Efficiency of ab-initio total energy calculations for metals and semiconductors using a plane-wave basis set. *Comput. Mater. Sci.* **1996**, *6*, 15-50.

(75) Perdew, J. P.; Burke, K.; Ernzerhof, M. Generalized gradient approximation made simple. *Phys. Rev. Lett.* **1996**, *77*, 3865-3868.

(76) Blöchl, P. E. Projector augmented-wave method. *Phys. Rev. B* **1994**, *50*, 17953-17979.

(77) Kresse, G.; Joubert, D. From ultrasoft pseudopotentials to the projector augmented-wave method. *Phys. Rev. B* **1999**, *59*, 1758-1775.

(78) Monkhorst, H. J.; Pack, J. D. Special points for Brillouin-zone integrations. *Phys. Rev. B* **1976**, *13*, 5188-5192.

(79) Cusinato, L.; Martinez-Prieto, L. M.; Chaudret, B.; del Rosal, I.; Poteau, R. Theoretical characterization of the surface composition of ruthenium nanoparticles in equilibrium with syngas. *Nanoscale* **2016**, *8*, 10974-10992.

(80) Martinez-Prieto, L. M.; Cano, I.; Marquez, A.; Baquero, E. A.; Tricard, S.; Cusinato, L.; del Rosal, I.; Poteau, R.; Coppel, Y.; Philippot, K.; Chaudret, B.; Campora, J.; van Leeuwen, P. W. N. M. Zwitterionic amidinates as effective ligands for platinum nanoparticle hydrogenation catalysts. *Chem. Sci.* **2017**, *8*, 2931-2941.

(81) Gonzalez-Gomez, R.; Cusinato, L.; Bijani, C.; Coppel, Y.; Lecante, P.; Amiens, C.; del Rosal, I.; Philippot, K.; Poteau, R. Carboxylic acid-capped ruthenium nanoparticles: experimental and theoretical case study with ethanoic acid. *Nanoscale* **2019**, *11*, 9392-9409.

(82) Maintz, S.; Deringer, V. L.; Tchougreeff, A. L.; Dronskowski, R. LOBSTER: A tool to extract chemical bonding from plane-wave based DFT. *J. Comput. Chem.* **2016**, *37*, 1030-1035.

(83) Gerber, I. C.; Poteau, R. Critical assessment of charge transfer estimates in non-covalent graphene doping. *Theor. Chem. Acc.* **2018**, *137*, 1-7.

(84) Cusinato, L.; del Rosal, I.; Poteau, R. Shape, electronic structure and steric effects of organometallic nanocatalysts: relevant tools to improve the synergy between theory and experiment. *Dalton Trans.* **2017**, *46*, 378-395.

(85) Hammer, B.; Noerskov, J. K. Electronic factors determining the reactivity of metal surfaces. *Surf. Sci.* **1995**, *343*, 211-220.

(86) Zaramello, L.; Albuquerque, B. L.; Domingos, J. B.; Philippot, K. Kinetic investigation into the chemoselective hydrogenation of α,β-unsaturated carbonyl compounds catalyzed by Ni(0) nanoparticles. *Dalton Trans.* **2017**, *46*, 5082-5090.

(87) Axet, M. R.; Conejero, S.; Gerber, I. C. Ligand effects on the selective hydrogenation of nitrobenzene to cyclohexylamine using ruthenium nanoparticles as catalysts. *ACS Appl. Nano Mater.* **2018**, *1*, 5885-5894.

(88) Garcia-Anton, J.; Axet, M. R.; Jansat, S.; Philippot, K.; Chaudret, B.; Pery, T.; Buntkowsky, G.; Limbach, H.-H. Reactions of olefins with ruthenium hydride nanoparticles: NMR characterization, hydride titration, and room-temperature C-C bond activation. *Angew. Chem., Int. Ed.* **2008**, *47*, 2074-2078.

(89) Bergounhou, C.; Blandy, C.; Choukroun, R.; Lecante, P.; Lorber, C.; Pellegatta, J.-L. Catalytic evidence of the core/shell structure of bimetallic Pd/Rh colloids. *New J. Chem.* **2007**, *31*, 218-223.

(90) Kelsen, V.; Meffre, A.; Fazzini, P.-F.; Lecante, P.; Chaudret, B. How to modulate catalytic properties in nanosystems: the case of iron-ruthenium nanoparticles. *ChemCatChem* **2014**, *6*, 1714-1720.

(91) Dinega, D. P.; Bawendi, M. A solution-phase chemical approach to a new crystal structure of cobalt. *Angew. Chem. Int. Ed.* **1999**, *38*, 1788-1791.

(92) Dassenoy, F.; Casanove, M.-J.; Lecante, P.; Verelst, M.; Snoeck, E.; Mosset, A.; Ely, T. O.; Amiens, C.; Chaudret, B. Experimental evidence of structural evolution in ultrafine cobalt particles stabilized in different polymers-From a polytetrahedral arrangement to the hexagonal structure. *J. Chem. Phys.* **2000**, *112*, 8137-8145.

(93) Margeat, O.; Respaud, M.; Amiens, C.; Lecante, P.; Chaudret, B. Ultrafine metallic Fe nanoparticles: synthesis, structure and magnetism. *Beilstein J. Nanotechnol.* **2010**, *1*, 108-118.

(94) Bonnefille, E.; Novio, F.; Gutmann, T.; Poteau, R.; Lecante, P.; Jumas, J.-C.; Philippot, K.; Chaudret, B. Tin-decorated ruthenium nanoparticles: a way to tune selectivity in hydrogenation reaction. *Nanoscale* **2014**, *6*, 9806-9816.

(95) Choukroun, R.; de Caro, D.; Chaudret, B.; Lecante, P.; Snoeck, E. H_2-induced structural evolution in non-crystalline rhodium nanoparticles. *New J. Chem* **2001**, *25*, 525-527.

(96) Novio, F.; Philippot, K.; Chaudret, B. Location and Dynamics of CO Co-ordination on Ru Nanoparticles: a Solid State NMR Study. *Catal. Lett.* **2010**, *140*, 1-7.

(97) Min, Y.; Nasrallah, H.; Poinsot, D.; Lecante, P.; Tison, Y.; Martinez, H.; Roblin, P.; Falqui, A.; Poteau, R.; del Rosal, I.; Gerber, I. C.; Hierso, J.-C.; Axet, M. R.; Serp, P. 3D Ruthenium nanoparticle covalent assemblies from polymantane ligands for confined catalysis. *Chem. Mater.* **2020**, *32*, 2365–2378.

(98) Lara, P.; Ayvali, T.; Casanove, M.-J.; Lecante, P.; Mayoral, A.; Fazzini, P.-F.; Philippot, K.; Chaudret, B. On the influence of diphosphine ligands on the chemical order in small RuPt nanoparticles: combined structural and surface reactivity studies. *Dalton Trans.* **2013**, *42*, 372-382.

(99) Lara, P.; Casanove, M.-J.; Lecante, P.; Fazzini, P.-F.; Philippot, K.; Chaudret, B. Segregation at a small scale: synthesis of core-shell bimetallic RuPt nanoparticles, characterization and solid state NMR studies. *J. Mater. Chem.* **2012**, *22*, 3578-3584.

(100) Jones, L. H. Infrared spectrum of solid $Ni(CO)_4$. *Spectrochim. Acta* **1963**, *19*, 1899-1904.

(101) Takahashi, Y.; Jacobs, R. L. A calculation of the magnetization of alloys of nickel with rhodium, ruthenium, iridium, and osmium. *J. Phys. F* **1982**, *12*, 517-528.

(102) Michelutti, B.; Perrier de la Bathie, R.; Du Tremolet de Lacheisserie, E.; Waintal, A. Magnetization, magnetocrystalline anisotropy, magnetostriction and elastic constants of a ruthenium-nickel single crystal. *Solid State Commun.* **1978**, *28*, 879-882.

(103) He, X.; Zhong, W.; Au, C.-T.; Du, Y. Size dependence of the magnetic properties of Ni nanoparticles prepared by thermal decomposition method. *Nanoscale Res. Lett.* **2013**, *8*, 1-10.

(104) Roy, A.; Srinivas, V.; Ram, S.; Rao, T. V. C. The effect of silver coating on magnetic properties of oxygen-stabilized tetragonal Ni nanoparticles prepared by chemical reduction. *J. Phys.: Condens. Matter* **2007**, *19*, 346220/346221-346220/346216.

(105) Herbois, R.; Noel, S.; Leger, B.; Bai, L.; Roucoux, A.; Monflier, E.; Ponchel, A. Cyclodextrins as growth controlling agents for enhancing the catalytic activity of PVP-stabilized Ru(0) nanoparticles. *Chem. Commun.* **2012**, *48*, 3451-3453.

(106) Herbois, R.; Noel, S.; Leger, B.; Tilloy, S.; Menuel, S.; Addad, A.; Martel, B.; Ponchel, A.; Monflier, E. Ruthenium-containing β-cyclodextrin polymer globules for the catalytic hydrogenation of biomass-derived furanic compounds. *Green Chem.* **2015**, *17*, 2444-2454.

(107) Pushkarev, V. V.; An, K.; Alayoglu, S.; Beaumont, S. K.; Somorjai, G. A. Hydrogenation of benzene and toluene over size controlled Pt/SBA-15 catalysts: elucidation of the Pt particle size effect on reaction kinetics. *J. Catal.* **2012**, *292*, 64-72.

(108) Somorjai, G. A.; Park, J. Y. Colloid science of metal nanoparticle catalysts in 2D and 3D structures. Challenges of nucleation, growth, composition, particle shape, size control and their influence on activity and selectivity. *Top. Catal.* **2008**, *49*, 126-135.

(109) Yu, Z.; Lu, X.; Wang, X.; Xiong, J.; Li, X.; Zhang, R.; Ji, N. Metal-catalyzed hydrogenation of biomass-derived furfural: particle size effects and regulation strategies. *ChemSusChem* **2020**.

(110) Pushkarev, V. V.; Musselwhite, N.; An, K.; Alayoglu, S.; Somorjai, G. A. High structure sensitivity of vapor-phase furfural decarbonylation/hydrogenation reaction network as a function of size and shape of Pt nanoparticles. *Nano Lett.* **2012**, *12*, 5196-5201.

(111) Sun, C.; Zeng, P.; He, M.; He, X.; Xie, X. Morphological effect of non-supported copper nanocrystals on furfural hydrogenation. *Catal. Commun.* **2016**, *86*, 5-8.

(112) Nakagawa, Y.; Nakazawa, H.; Watanabe, H.; Tomishige, K. Total hydrogenation of furfural over a silica-supported nickel catalyst prepared by the reduction of a nickel nitrate precursor. *ChemCatChem* **2012**, *4*, 1791-1797.

(113) Young, C. L.; Editor: *Solubility data series, Vol. 5/6: hydrogen and deuterium*, 1981.

(114) Brunner, E. Solubility of hydrogen in 10 organic solvents at 298.15, 323.15, and 373.15 K. *J. Chem. Eng. Data* **1985**, *30*, 269-273.

(115) Trinh, T.-K.-H.; de Hemptinne, J.-C.; Lugo, R.; Ferrando, N.; Passarello, J.-P. Hydrogen solubility in hydrocarbon and oxygenated organic compounds. *J. Chem. Eng. Data* **2016**, *61*, 19-34.

(116) Leng, F.; Gerber, I. C.; Axet, M. R.; Serp, P. Selectivity shifts in hydrogenation of cinnamaldehyde on electron-deficient ruthenium nanoparticles. *C. R. Chim.* **2018**, *21*, 346-353.

(117) Wu, D.; Hernandez, W. Y.; Zhang, S.; Vovk, E. I.; Zhou, X.; Yang, Y.; Khodakov, A. Y.; Ordomsky, V. V. In situ generation of Bronsted acidity in the Pd-I bifunctional catalysts for selective reductive etherification of carbonyl compounds under mild conditions. *ACS Catal.* **2019**, *9*, 2940-2948.

(118) Wang, X.; Weng, Y.; Zhao, X.; Xue, X.; Meng, S.; Wang, Z.; Zhang, W.; Duan, P.; Sun, Q.; Zhang, Y. Selective hydrogenolysis and hydrogenation of furfuryl alcohol in the aqueous phase using Ru-Mn-based catalysts. *Ind. Eng. Chem. Res.* **2020**, *59*, 17210-17217.

(119) Zhang, B.; Zhu, Y.; Ding, G.; Zheng, H.; Li, Y. Selective conversion of furfuryl alcohol to 1,2-pentanediol over a Ru/MnOx catalyst in aqueous phase. *Green Chem.* **2012**, *14*, 3402-3409.

(120) Goetz, D.; Lucas, M.; Claus, P. C-O bond hydrogenolysis vs. C=C group hydrogenation of furfuryl alcohol: towards sustainable synthesis of 1,2-pentanediol. *React. Chem. Eng.* **2016**, *1*, 161-164.

(121) Nakagawa, Y.; Tomishige, K. Total hydrogenation of furan derivatives over silica-supported Ni-Pd alloy catalyst. *Catal. Commun.* **2010**, *12*, 154-156.

(122) del Rosal, I. a. P. R.: Sabatier principle and surface properties of small ruthenium nanoparticles and clusters: case studies. In *Nanoparticles in catalysis*; Roucoux, K. P. a. A., Ed., 2021; pp 331-351.

(123) Moraru, I.-T.; Martinez-Prieto, L. M.; Coppel, Y.; Chaudret, B.; Cusinato, L.; del Rosal, I.; Poteau, R. Joint theoretical/experimental highlight on the formation of carbides on Ru nanoparticles during CO hydrogenation. *Nanoscale* **2021**.

(124) Leng, F.; Gerber, I. C.; Lecante, P.; Bentaleb, A.; Munoz, A.; Illescas, B. M.; Martin, N.; Melinte, G.; Ersen, O.; Martinez, H.; Axet, M. R.; Serp, P. Hexakis [60]fullerene adduct-mediated covalent assembly of ruthenium nanoparticles and their catalytic properties. *Chem. - Eur. J.* **2017**, *23*, 13379-13386.

(125) Taglang, C.; Martinez-Prieto, L. M.; del Rosal, I.; Maron, L.; Poteau, R.; Philippot, K.; Chaudret, B.; Perato, S.; Sam Lone, A.; Puente, C.; Dugave, C.; Rousseau, B.; Pieters, G. Enantiospecific C-H activation using ruthenium nanocatalysts. *Angew. Chem., Int. Ed.* **2015**, *54*, 10474-10477.

(126) Pfeifer, V.; Certiat, M.; Bouzouita, D.; Palazzolo, A.; Garcia-Argote, S.; Marcon, E.; Buisson, D.-A.; Lesot, P.; Maron, L.; Chaudret, B.; Tricard, S.; del Rosal, I.; Poteau, R.; Feuillastre, S.; Pieters, G. Hydrogen isotope exchange catalyzed by Ru nanocatalysts: labelling of complex molecules containing N-heterocycles and reaction mechanism insights. *Chem. - Eur. J.* **2020**, *26*, 4988-4996.

(127) Pery, T.; Pelzer, K.; Buntkowsky, G.; Philippot, K.; Limbach, H.-H.; Chaudret, B. Direct NMR evidence for the presence of mobile surface hydrides on ruthenium nanoparticles. *ChemPhysChem* **2005**, *6*, 605-607.

(128) Truflandier, L. A.; Del Rosal, I.; Chaudret, B.; Poteau, R.; Gerber, I. C. Where does hydrogen adsorb on Ru nanoparticles? A powerful joint ^{2}H MAS-NMR/DFT approach. *ChemPhysChem* **2009**, *10*, 2939-2942.